UPPSALA
UNIVERSITET

Digital Comprehensive Summaries of Uppsala Dissertations from the Faculty of Science and Technology 1510

Electronic Structure and Atomistic Spin Dynamics of Nanostructured Materials

DEBORA C. M. RODRIGUES

ACTA
UNIVERSITATIS
UPSALIENSIS
UPPSALA
2017

ISSN 1651-6214
ISBN 978-91-554-9903-7
urn:nbn:se:uu:diva-319994

Dissertation presented at Uppsala University to be publicly examined in Seminar room, Federal University of Pará, Av. Augusto Correa, 01., Belém, Friday, 2 June 2017 at 13:15 for the degree of Doctor of Philosophy. The examination will be conducted in English. Faculty examiner: Prof. Helena Petrilli (University of São Paulo).

Abstract
Rodrigues, D. C. M. 2017. Electronic Structure and Atomistic Spin Dynamics of Nanostructured Materials. *Digital Comprehensive Summaries of Uppsala Dissertations from the Faculty of Science and Technology* 1510. 39 pp. Uppsala: Acta Universitatis Upsaliensis. ISBN 978-91-554-9903-7.

The theoretical studies of several magnetic materials are presented in this thesis. To each of them, it was investigated the electronic structure, by means of density functional theory calculations, and/or magnetization dynamics, in the context of atomistic spin dynamics (ASD).

For bulk properties, we evaluate the magnon spectra of the heavy rare earths (Gd, Tb, Dy, Ho, Er, and Tm), using the exchange parameters and magnetic moments from first-principles calculations in ASD simulations. Additionally, we performed Monte Carlo simulations that nicely reproduced the qualitative trend of lowering of the critical temperatures across the series. Next, we discuss about the microscopic mechanism of the vanishingly low magnetic anisotropy of Permalloy using the concept of the orbital moment anisotropy for Fe and Ni atoms in the alloy. Turning to surface magnetism, we discuss the use of exchange parameters computed by a noncollinear formalism for 6 monolayers of Fe on the Ir(001) substrate, in order to have a more accurate description of magnons at finite temperature and to obtain good comparison with experimental data. Besides that, we also studied surface magnons on 3 and 9 Ni monolayers on Cu(001) and Cu(111) in order to track the significant surface and/or interface effects and contrast it to properties that are fcc Ni bulk-like. Likewise, we used the Monte Carlo method to estimate the critical temperatures of Ni surfaces and compared with experimental data. Finally, in the field of low dimensional magnetism, we present the ab-initio calculations for the electronic structure of Cr nanostructures of diverse geometries adsorbed on the Pd(111) surface, with focus on the formation of non-collinear spin configurations, either due to geometric frustration or the spin-orbit coupling provided by the substrate.

Debora C. M. Rodrigues, Department of Physics and Astronomy, Materials Theory, Box 516, Uppsala University, SE-751 20 Uppsala, Sweden.

ISSN 1651-6214
ISBN 978-91-554-9903-7
urn:nbn:se:uu:diva-319994 (http://urn.kb.se/resolve?urn=urn:nbn:se:uu:diva-319994)

To my beloved family

List of papers

This thesis is based on the following papers, which are referred to in the text by their Roman numerals.

I I. L. M. Locht, Y. O. Kvashnin, **D. C. M. Rodrigues**, M. Pereiro, A. Bergman, L. Bergqvist, A. I. Lichtenstein, M. I. Katsnelson, A. Delin, A. B. Klautau, B. Johansson, I. Di Marco, and O. Eriksson
Standard model of the rare earths analyzed from the Hubbard I approximation.
Phys. Rev. B **94**, 085137 (2016)

II **D. C. M. Rodrigues**, A. B. Klautau, A. Edström, J. Rusz, L. Nordström, M. Pereiro, B. Hjörvarsson, and O. Eriksson.
Magnetic anisotropy in Permalloy: hidden quantum mechanical features.
Submitted to PRB (2017)

III **D. C. M. Rodrigues**, A. Szilva, A. B. Klautau, A. Bergman, O. Eriksson, and C. Etz
Finite-temperature interatomic exchange and magnon softening in Fe overlayers on Ir(001).
Phys. Rev. B **94**, 014413 (2016)

IV **D. C. M. Rodrigues**, S. Keshavarz, Y. O. Kvashnin, A. B. Klautau, O. Eriksson, B. Hjörvarsson, and A. Bergman.
Surface magnons and critical temperatures of Ni surfaces on Cu.
In manuscript

V **D. C. M. Rodrigues**, M. Pereiro, A. Bergman, O. Eriksson, and A. B. Klautau
First-principles theory of electronic structure and magnetism of Cr nano-islands on Pd(111).
J. Phys.: Condens. Matter **29**, 025807 (2017).

During the work in this thesis the following works were also made, but are not included in the thesis.

VI L. Nordström, A. Edström, **D. C. M. Rodrigues**, A. B. Klautau, J. Rusz, and O. Eriksson.
New permanent magnets; what to look for, and where.
in manuscript

VII S. Keshavarz, Y. O. Kvashnin, **D. C. M. Rodrigues**, M. Pereiro, I. Di Marco, C. Autieri, L. Nordström, I. V. Solovyev, B. Sanyal, and O. Eriksson
Exchange interactions of $CaMnO_3$ in the bulk and at the surface.
*Phys. Rev. B **95**, 115120 (2017)*

Reprints were made with permission from the publishers.

Contents

1. Introduction

The early observations of the magnetic phenomena date back to ancient times. It can be seen not only in Greek and Chinese writings but also in the archaeological remains of pre-Columbian civilizations [1]. These civilizations reported the use of magnetite stones, an iron oxide naturally magnetized with the ability to attract iron. Centuries later, the first memorable application of magnetism has emerged: the sea-navigation compasses. Therefore, the magnetism contributed to the expansion of the “known world" in the fifteenth century by European navigators.

The first scientific essay on magnetism is attributed to William Gilbert by his book “De Magnete" (1600). There was launched the idea that the Earth has its own magnetic field similar to the natural magnets, and, for this reason the compass needle align itself to the earth’s field. At this moment Gilbert has already introduced the concept of magnetic and electric *effluvium* (field).

After three centuries of theoretical proposals and empirical observations, the scientific research of magnetism comes to the nineteenth century with the discovery of electromagnetism and its connection to light in the experimental works of Hans-Christian Oersted (the magnetic field produced by an electric current), André-Marie Ampère (equivalence between an electric coil and a magnet) and Michael Faraday (electromagnetic induction and the magneto-optical effect). Nonetheless, the most precious jewel of the scientific knowledge in the nineteenth century was developed in 1864, by James Clerk Maxwell, with the formulations of the laws of electrodynamics. Complementary, many of the experimental techniques known at that time give birth to new technologies: electric motors and generators, telephones and telegraphs stated to be part of the everyday life!

In the twentieth century, the quantum mechanics revealed the deepest secret about magnets: the spin of the electron. Many names can be mentioned, but Pauli, Dirac, Fermi, Heisenberg, Bloch and Néel definitely have the most influential contributions to the theory of metals and magnetism. Also the development of the density functional theory by Hohenberg and Kohn [2] was a turning point in theoretical predictions on materials science. Besides that, the first recordings in magnetic media (magnetic tapes and floppy-disks) appeared in the 1930’s. However, the new breakthrough in terms of technology came in 1988 with the discovery of the giant magnetoresistance effect (GMR)[3, 4] and the birth of spintronics at the end of the century. This enabled the development of faster devices for data storage and processing.

Meantime, "*hard drives are getting so big they're almost scary. Who really needs 8 gigabytes of storage (...)?*"[1], that was the concern in 1998. It is been almost 20 years since the hard drive disks using GMR heads were released to the market and, nowadays, the information storage units turned into Terabytes! This just reveals the effort of the scientific community to find new materials and solutions for magnetic storage. Now, the horizon is to stabilize bits with the fewest possible number of atoms and optimization of processing, associated with the lower energy expenditure.

The later developments in experimental techniques have a significant role for the research on magnetic materials. For example, the scanning tunneling microscope (STM) [6, 7] enables the topological mapping of the surface on atomic scale and the manipulation of atoms. It also has some particular applications, such as spin-polarized STM (SP-STM) [8], which provides information about noncollinear magnetic textures [9, 10, 11], and the scanning tunnelling spectroscopy (STS) technique, which by means of the measured differential conductivity it is possible to distinguish the topography, electronic structure and magnetism of a sample [12, 13], as well as measure the exchange coupling between atoms [14]. It is also possible to investigate the collective excitations of the spins in a magnetic material (magnons) by means of the Inelastic Neutron Scattering (INS) techniques [15, 16, 17] and Spin Polarized Electron Energy Loss Spectroscopy (SPEELS) [18].

In fact, the use of neutron and electron scattering techniques to measure the magnon dispersion relation provide the access to valuable information about the studied system such as the exchange coupling, magnetic anisotropy and possibly the Dzyaloshinskii-Moriya interaction. Once the material is characterized and the relevant interactions are known, this knowledge can be applied subsequently to create devices, such as a magnonic transistors [19]. As other examples, recent experimental works showed that are the possibility of stabilizing bits composed of 12 atoms at low temperature [20], as well as the construction of nanodevices to perform logical operations using only spins [21].

In fact, "*there's plenty of room at the bottom*" as Richard Feynman pointed out in 1959... and still! The studies show that despite all the advances made, the understanding of magnetism in matter from the basic knowledge to the applications of high density magnetic storage and spintronic/magnonic devices are a daily challenge for scientists.

Therefore, in view of these perspectives and high scientific interest in the field of nanomagnetism, in this thesis are presented theoretical studies of electronic structure and atomistic spin dynamics of magnetic materials, done by means of first principles calculations using the Real-Space Linear Muffin-Tin Orbital within the Atomic Sphere Approximation (RS-LMTO-ASA) method and Uppsala Atomistic Spin Dynamics code (UppASD).

[1] From "When it comes to hard drives, size is everything" by Stan Miastkowski (June 12, 1998) [5].

The RS-LMTO-ASA [22, 23, 24] is based on the density functional theory (DFT) [2, 25], an effective and widely used theory for solving many interacting electron problems. The mentioned method is also a real-space generalization of the original k-space LMTO-ASA method, solving the eigenvalue problem in real space, which simplify the study of systems with low symmetry. The DFT, the LMTO-ASA method and the RS-LMTO-ASA are presented in Chapter 2.

Chapter 3 is dedicated to the magnetic ordering. The origin of the atomic magnetic moment and the band theory of magnetism are shown, followed by the different energy contributions for the spin Hamiltonian: the pair interactions between atomic spins, as the Heisenberg exchange and Dzyaloshinsky-Moriya interactions, and the magnetocrystalline anisotropy. The collinear and noncollinear magnetism is also discussed.

In Chapter 4 the Landau-Lifshitz-Gilbert (LLG) equation is discussed in the context of atomistic spin dynamics. The study of the dynamical properties of the atomic spin is described by the stochastic version of LLG equation, as implemented in the UppASD package [26, 27]. The theory of spin waves and the Monte Carlo method are also discussed here.

Chapter 5 contains the introduction to the studies presented in this thesis:

- Paper **I** where we describe the $4f$ electrons as core levels in the electronic structure calculations and estimate the critical temperatures and magnon spectra of the heavy rare earths (Gd, Tb, Dy, Ho, Er, and Tm);
- Paper **II** contains the discussion about the microscopic mechanism of the vanishingly low magnetic anisotropy of Permalloy using the concept of the orbital moment anisotropy for Fe and Ni atoms in the alloy;
- Paper **III** discuss the use of exchange parameters computed by the noncollinear formalism [28] for 6 monolayers of Fe on the Ir(001) substrate – Fe_6/Ir(001), in order to have a more accurate description of magnons at finite temperature in comparison with experimental data;
- Paper **IV** deals with surface magnons on Ni_n/Cu(001) and Ni_n/Cu(111), with $n = 3, 9$ in order to track the significant surface and/or interface effects and contrast this to properties that are fcc Ni bulk-like. Likewise, we used the Monte Carlo method in order to calculate critical temperatures and compare with experimental data;
- Paper **V** presents the ab-initio calculations for the electronic structure of Cr nanostructures of diverse geometries adsorbed on the Pd(111) surface, with focus on the formation of non-collinear spin configurations, either due to geometric frustration or the spin-orbit coupling interaction provided by the substrate.

Therefore, the studies presented here comprise several materials in solid state physics. From the bulk properties, with elemental rare-earths and Fe-

Ni random alloy, to surface properties, exemplified by Fe and Ni thin films supported on top of non-magnetic substrates, as well as nanostructures adsorbed on a substrate with considerable spin-orbit interaction, represented by Cr nanoislands. Finally, I end up with the summary and perspectives based in the presented finds.

2. Density functional theory

2.1 The many body problem

The macroscopic physical properties of the materials can be well described from the investigation of events at the microscopic scale, especially those related to the quantum states of the electrons in the crystalline lattice. According to quantum mechanics, a priori, we can solve the time independent Schrödinger equation,

$$\mathscr{H}\Psi_i(\vec{r},\vec{R}) = E_i\Psi_i(\vec{r},\vec{R}), \tag{2.1}$$

to obtain the many body eigenstates $\Psi_i(\vec{r},\vec{R})$ and the eigenvalues E_i for a crystalline system, with $\vec{r}$ and $\vec{R}$ been the coordinates of the electrons and nuclei, respectively. The Hamiltonian operator $\mathscr{H}$ contains the interactions for electrons and nuclei, in Rydberg atomic units,[1]

$$\mathscr{H} = -\sum_I \frac{\nabla_I^2}{2M_I} - \sum_i \nabla_i^2 + \sum_{J\neq I} \frac{Z_I Z_J}{|\vec{R}_I - \vec{R}_J|} + \sum_{j\neq i} \frac{1}{|\vec{r}_i - \vec{r}_j|} - \sum_{I,i} \frac{2Z_I}{|\vec{R}_I - \vec{r}_i|}, \tag{2.2}$$

where small (capital) letters stand for electron (nuclei), as in $\vec{r}_i$ and $\vec{R}_I$. The element specific information is represented by the atomic number Z and mass of the nuclei M_I. In the right hand side of Eq. 2.2, we find the kinetic energies of nuclei and electrons with $\nabla = \frac{\partial}{\partial r}$, as well as the Coulomb interactions of nucleus-nucleus, electron-electron, and electron-nucleus, respectively. The exact solution of the many-body problem is restricted to a few cases, specially due to the coupling between nuclear-electronic movements that hinders the total wave-function factorization. The most basic approach is to consider the difference of time-scales of nuclei and electrons movement, which is known as the adiabatic approximation of Born-Oppenheimer [29, 30]. Due to large difference in mass, the electron is several orders of magnitude faster than the nuclei. For example, the ratio of electron-nuclei mass for the hydrogen atom is $1/1836$. Therefore, it is possible a description in which the electrons respond instantaneously to variations in the wave function of the nucleus. Likewise, the inverse of the nuclear mass $1/M_I$ is small, which allows us to neglect the nuclear kinetic energy in Eq. 2.2,

$$\mathscr{H} = -\sum_i \nabla_i^2 + \sum_{j\neq i} \frac{1}{|\vec{r}_i - \vec{r}_j|} - \sum_{I,i} \frac{2Z_I}{|\vec{R}_I - \vec{r}_i|}, \tag{2.3}$$

[1] Which means $\hbar = 1$, $e^2 = 2$ and $m_i = 1/2$

and the total wave function can be written in the form

$$\Psi(\vec{r},\vec{R}) = \psi_{nuc}(\vec{R})\ \psi_{ele}(\vec{R},\vec{r}), \tag{2.4}$$

where $\psi_{nuc}(\vec{R})$ is related to the nuclear part, and $\psi_{ele}(\vec{R},\vec{r})$ the electron part that remains in the same steady state of the electronic Hamiltonian. Thus, the electronic problem is reduced to the calculation of electron steady states, moving in the electrostatic field of the fixed nuclei. Despite this, Eq. 2.3 continue a complex many electron problem with exact solution restricted to a few systems. Hence, other approximations are necessary for analytical treatments.

2.2 Density functional theory

A feasible and widespread solution is to map the many electron problem into a single particle problem by promoting the electronic density $n(\vec{r})$ to a variable and turn all physical observables written in terms of it. Known as the density functional theory (DFT), this solution was first proposed in the works of Thomas [31], Fermi [32] and Dirac [33] however, it was mathematically established by Hohenberg and Kohn through their theorems [2]. Then, Kohn and Sham [25] propose a formulation as a system of independent particles with interacting electronic density, establishing a self-consistent method to obtain the ground state density, $n_0(\vec{r})$.

From the theorems of Hohenberg and Kohn [2], for an interacting electrons system subject to an external potential V, follows that:

The Hohenberg-Kohn theorems

1. The ground state density $n_0(\vec{r})$ determines uniquely the external potential V, except for a constant;
2. The energy functional $E[n(\vec{r})]$ is minimized only when the density $n(\vec{r}) = n_0(\vec{r})$, giving the exact ground state energy.

For practical purpose, Kohn and Sham proposed to use a effective potential V_{eff} as a way to compute the right ground state density [25]. Therefore, the multi-electronic Hamiltonian in Eq. 2.3 can be modified, resulting in a new eigenvalue equation,

$$[-\nabla^2 + V_{eff}(\vec{r})]\psi_i(\vec{r}) = E_i\psi_i(\vec{r}), \tag{2.5}$$

known as the Kohn-Sham equations, where $\psi_i(\vec{r})$ is the single particle wavefunction and $V_{eff}(\vec{r})$ is given by

$$V_{eff}(\vec{r}) = V_{ext} + 2\int \frac{n(\vec{r})}{|\vec{r}-\vec{r'}|}d\vec{r'} + V_{XC}(\vec{r}). \tag{2.6}$$

Thus, the problem is reduced to the solution of subsystems of a single particle subject to an effective field, Eq. 2.6, composed by V_{ext} generated by the nuclei, the Hartree term generated by electrons in the neighborhood $\vec{r}'$, and the exchange-correlation potential V_{XC} with quantum mechanical origin.

The Kohn-Sham (KS) equations are solved in an iterative and self-consistent (SC) process, given an initial electron density $n_u(\vec{r})$. The SC scheme is summarized below.

Kohn-Sham self-consistent scheme

1. obtain the effective potential as a functional of $n_u(\vec{r})$;
2. solve the KS equations to obtain the eigenfunctions $\psi_{i,u}(\vec{r})$;
3. compute the new electronic density $n_{u+1}(\vec{r}) = \sum_i |\psi_{i,u}(\vec{r})|^2$;
4. if $\frac{n_{u+1}}{n_u} >$ criteria $\rightarrow$ return to 1.

Usually the iterations cycles continue using new initial density, that is a combination of $n_{u+1}(\vec{r})$ and $n_u(\vec{r})$ and occurs until the resulting density differ from the initial one by a established threshold (self-consistency process).

2.3 Exchange-correlation functional in local density approximation

The V_{XC} derives from the electron's intrinsic properties – charge and spin. Antecedent to DFT, the Hartree-Fock theory accounts for the exact exchange part, a consequence of Fermi statistics via the Slater determinant. Aside from that, the electrons with anti-parallel spins move in a completely uncorrelated fashion however, the Coulomb repulsion prevents them to occupy regions extremely close to each other (Coulomb correlation). This type of correlation effect is neglected in Hartree-Fock, though present in the V_{XC} in the DFT level.

Despite of the fact that the V_{XC} term carries the many-body effects, it does not have a closed analytical expression yet. For that, the exchange and correlation effects are treated by approximations in the study of materials. Among the functionals reported are the local density approximation - LDA [25, 34], generalized gradient approximation - GGA [35, 36], hybrid functionals as B3LYP [37], and Hubbard corrected functional - DFT+U [38].

The local density approximation (LDA) treat the inhomogeneous system of many electrons as a set of subsystems (with homogeneous electron gas characteristics) interacting with each other. Complementary, for spin-polarized systems the local spin density approximation (LSDA) [34] was developed. Thus, assuming that $n(\vec{r})$ has smooth variation in a region close to $\vec{r}$, the exact exchange-correlation energy functional can be approximated by the first term

of its expansion [25]

$$E_{xc}^{LSDA}[n^{\uparrow},n^{\downarrow}] = \int n(\vec{r})\, \varepsilon_{xc}^{hom}([n^{\uparrow}],[n^{\downarrow}],\vec{r})\, d\vec{r}, \tag{2.7}$$

where $n^{\uparrow}(\vec{r})$ and $n^{\downarrow}(\vec{r})$ stands for majority ($\uparrow$) and minority ($\downarrow$) spin densities. The ε_{xc}^{hom} is the exchange-correlation energy per particle in a homogeneous spin-polarized electron gas at $\vec{r}$ and the E_{xc}^{LSDA} is a functional of the density in a region around $\vec{r}$ (local characteristic).

The expression of the exchange-correlation potential $V_{xc}(\vec{r})$ is given by the functional derivative of Eq. 2.7

$$V_{xc}^{\sigma}(\vec{r}) = \frac{\delta\left(n(\vec{r})\, \varepsilon_{xc}^{hom}([n^{\uparrow}],[n^{\downarrow}],\vec{r})\right)}{\delta n^{\sigma}(\vec{r})} \tag{2.8}$$

with $\sigma = \uparrow$ or $\downarrow$.

The density $n([n^{\uparrow}],[n^{\downarrow}],\vec{r})$ could be replaced by the generalized density matrix $\boldsymbol{\rho}(\vec{r})$ [34], written as

$$n(\vec{r}) \rightarrow \boldsymbol{\rho}(\vec{r}) = \frac{n(\vec{r})}{2}\mathbb{1} + \frac{\boldsymbol{m}(\vec{r})}{2}\boldsymbol{\sigma} \tag{2.9}$$

where $\mathbb{1}$ is a unitary matrix 2×2, $\boldsymbol{m}$ the magnetization density and $\boldsymbol{\sigma}$ the Pauli spin matrices. The KS wave-functions $\boldsymbol{\psi}_i(\vec{r})$ are then extended to a spinor representation,

$$\boldsymbol{\psi}_i(\vec{r}) = \begin{pmatrix} \alpha_i(\vec{r}) \\ \beta_i(\vec{r}) \end{pmatrix} \tag{2.10}$$

with $\alpha_i(\vec{r})$ and $\beta_i(\vec{r})$ the spin projections. Hence, the $\boldsymbol{\rho}(\vec{r})$ assumes the form

$$\boldsymbol{\rho}(\vec{r}) = \sum_i \begin{pmatrix} |\alpha_i(\vec{r})|^2 & \alpha_i(\vec{r})\beta_i^*(\vec{r}) \\ \alpha_i^*(\vec{r})\beta_i(\vec{r}) & |\beta_i(\vec{r})|^2 \end{pmatrix}. \tag{2.11}$$

Thus, the charge and spin part of the density are expressed in terms of $\boldsymbol{\psi}_i(\vec{r})$, accordingly to Eq. 2.9, as

$$n(\vec{r}) = Tr[\boldsymbol{\rho}(\vec{r})] = \sum_i |\boldsymbol{\psi}_i(\vec{r})|^2 \quad \text{(charge)} \tag{2.12}$$

and

$$\boldsymbol{m}(\vec{r}) = \sum_i \boldsymbol{\psi}_i^{\dagger}(\vec{r})\boldsymbol{\sigma}(\vec{r})\boldsymbol{\psi}_i(\vec{r}) \quad \text{(spin)}. \tag{2.13}$$

The external potential V_{ext} also assumes the 2×2 matrix form and the Kohn-Sham equation, Eq. 2.5, is generalized to

$$[-\nabla^2 + V_{eff}^{\sigma}(\vec{r})]\boldsymbol{\psi}_i^{\sigma}(\vec{r}) = E_i^{\sigma}\boldsymbol{\psi}_i^{\sigma}(\vec{r}), \tag{2.14}$$

for the spin polarized problem. Considering that the potential V_{eff}^{σ} admit the separation into non-magnetic and magnetic part, $\boldsymbol{b}$ and V_{NM} respectively, the Kohn-Sham Hamiltonian in the LSDA is

$$\mathscr{H}_{KS} = \left(-\nabla^2 + V_{NM}\right)\mathbb{1} + \boldsymbol{b}\cdot\boldsymbol{\sigma}. \tag{2.15}$$

The Eq. 2.15 is diagonal in the collinear spin case (when there is a global quantization direction), then the KS wave-functions for distinct spin channel do not hybridize and can be solved independently.

In all DFT calculations contained in this thesis, the exchange-correlation functional was set to LSDA. Thus, we will not further discuss the other exchange correlation functionals (more information can be found in the listed references).

2.4 Spin-orbit coupling

In the electronic structure context, the spin-orbit coupling (SOC) carries the relativistic character. Therefore, to investigate quantities as the orbital moments and magnetocrystalline anisotropy, it is necessary to include the SOC term into the Hamiltonian.

The fully-relativistic treatment can be achieved by solving the Dirac equation or consider the SOC as a perturbation term added to Eq. 2.15,

$$\mathscr{H} = \mathscr{H}_{KS} + \xi\ \boldsymbol{L}\cdot\boldsymbol{S}. \tag{2.16}$$

Here the $\xi \propto \frac{1}{r}\frac{\partial V}{\partial r}$ is the SOC parameter, which is also proportional to the atomic number Z. Therefore, by construction, the SOC term is more relevant for heavy atoms [39].

In all DFT calculations contained in this thesis, the SOC term was treated as a perturbation, accordingly to Eq. 2.16.

2.5 LMTO basis

After discussing the basic features of DFT, one would think how to compute the KS orbitals and consequently the ground state density. Apart from the suitable approximation for V_{xc}, it is also needed to select a basis set to expand the KS orbitals $\psi_i(\vec{r})$ and solve Eq. 2.14. Since it has a Schrödinger-like form, the natural procedure is to write ψ_i as a linear combination of basis functions $\{\chi_j\}$,

$$\psi_i = \sum_j \chi_j\ u_{j,i}\ , \tag{2.17}$$

where $u_{j,i}$ are the expansion coefficients. Thus, the eigenvalue equation turns

$$(\boldsymbol{H} - E\ \boldsymbol{O})\boldsymbol{u} = 0, \tag{2.18}$$

with $\boldsymbol{u}$ the coefficients matrix $u_{j,i}$ and $\boldsymbol{O}$ the overlap matrix. The Hamiltonian matrix $\boldsymbol{H}$ and $\boldsymbol{O}$ are given by the matrix elements

$$H_{j,k} = \langle \chi_j | (-\nabla^2 + V_{eff}) | \chi_k \rangle \tag{2.19}$$

and

$$O_{j,k} = \langle \chi_j | \chi_k \rangle. \tag{2.20}$$

The form of the basis functions $\{\chi_j\}$ is constrained to the most appropriated type of functions to represent each range of problems. For example, wave function based approaches, as the contracted Gaussian functions [40], are suitable to investigate the electronic structure of molecules and small metal clusters. In case of crystalline structures, plane waves basis are known by their simple form and often implemented in association with pseudopotentials [41]. Periodic systems are also well described by augmented methods such as augmented plane waves formulation [42], Green's functions method [43] or linear muffin-tin orbitals methods [44].

In this thesis, the $\{\chi_j\}$ basis set is a linear combination of muffin-tin orbitals (LMTO), following the LMTO formalism [44]. In this picture, the effective potential inside the atomic regions is approximated to a symmetric spherical potential $V_{eff}(\vec{r}) \rightarrow V_R(r)$, while it kept a constant (V_0) in the interstitial region (see Fig. 2.1). Here the atomic sphere approximation (ASA) is applied, meaning that the Wigner-Seitz cell is approximated with a sphere with radius s (or MT radius). For simplicity, in order to introduce the basis functions, it is convenient to consider zero kinetic energy in the region outside of the atomic sphere ($r > s$).

Now, imagine an isolated muffin-tin well, as in Fig. 2.1b, where the MT potential is delimited by s and centred around the atom placed at position $\vec{R}$. In this case, Eq. 2.14 turns into

$$[-\nabla^2 + V_R(r_R) - E_i]\psi_i(\vec{r}_R, E) = 0, \; r < s \tag{2.21}$$

and

$$-\nabla^2 \psi_i(\vec{r}_R) = 0, \qquad r > s \tag{2.22}$$

with $\vec{r}_R = \vec{r} - \vec{R}$ and neglecting the σ index. The MT potential is spherical symmetric and admit the product of radial and angular functions as solution. Thus, Eq. 2.21 has the solution

$$\psi_i(\vec{r}_R, E) = \phi_{R,l}(r, E) Y_L(\hat{r}). \tag{2.23}$$

The Eq. 2.22 is the Laplace equation, with asymptotic solutions

$$\begin{aligned} J_{R,L}(\vec{r}_R) &= \left(\frac{r_R}{s}\right)^l \frac{1}{2(2l+1)} Y_L(\hat{r}_R) \quad (r_R \rightarrow 0) \\ &= j_{R,L}(r_{R'}) \, Y_L(\hat{r}_R) \end{aligned} \tag{2.24}$$

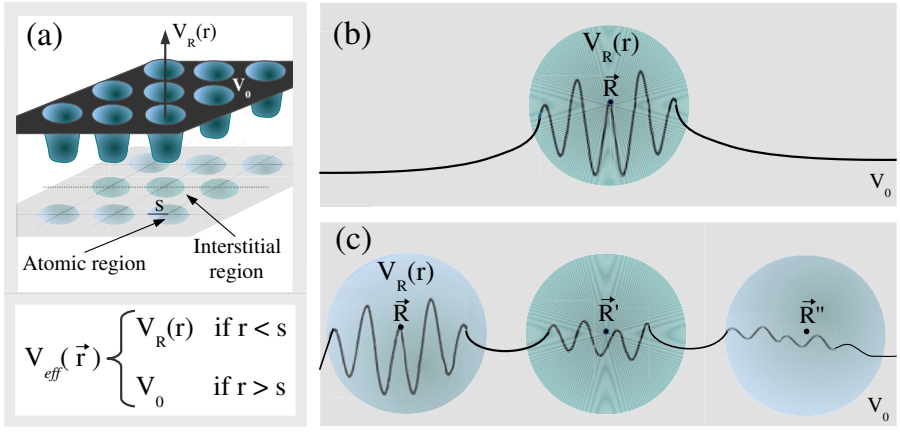

Figure 2.1. (a) Muffin-tin potential with the basis functions in the case of (b) an isolated muffin-tin potential at $\vec{R}$ or (c) in a crystalline environment with periodic muffin-tin potentials at $\vec{R}'$, $\vec{R}''$, $\vec{R}'''$, etc.

and

$$\begin{aligned} K_{R,L}(\vec{r}_R) &= \left(\frac{r_R}{s}\right)^{-(l+1)} Y_L(\hat{r}_R) \qquad (r_R \to \infty) \\ &= k_{R,L}(r_R)\, Y_L(\hat{r}_R) \end{aligned} \tag{2.25}$$

where Y_L are the spherical harmonics, with $L = \{l, m\}$ representing orbital l and magnetic m quantum numbers.

We assume for a while that we know the one-electron solution inside the atomic spheres (Eq. 2.23) and focus on the solutions of the Laplace equation. For a single MT, the Eq. 2.25 has prolongation for all space outside the sphere R, (see Fig. 2.1b). In case of an arrangement of spheres in a crystal lattice, Fig. 2.1c, it is sufficient to correct the $K_{R,L}$ in its domain parts that are now occupied by the other atomic spheres centred at the sites $\vec{R}' \neq \vec{R}$. Therefore, the $K_{R,L}$ are defined as a set of envelope functions. Note that Eq. 2.25 diverges at the origin, for this reason it only describes the behavior $\chi^0_{R,L}$ in the interstitial area and at the spheres boundary.

The $K_{R,L}$ can be expanded from sites $\vec{R}'$ into the neighboring spheres $\vec{R}$, creating a complete set using Eq. 2.24. Hence, we can define $K^0_{R,L}$ as

$$K^0_{R,L} = -\sum_{R',L'} S^0_{R',L';\,R,L}\, J^0_{R',L'}(r_{R'}), \tag{2.26}$$

where $S^0_{R',L';\,R,L}$ gathers the expansion coefficients of $K^0_{R,L}$ around R' and contains structural information, with $(|\vec{R} - \vec{R}'|)^{-1}$ dependence. For that reason it

is called the canonical structure matrix.[2] Thus, the envelope function defined in all space, $K^{\infty}_{R,L}$, using Eq. 2.25 and Eq. 2.26, is

$$\begin{aligned} K^{\infty}_{R,L} &= K_{R,L} + K^{0}_{R,L} \\ &= k_{R,l}(r_R)\, Y_L(\hat{r}_R) - \sum_{R',L'} j^{0}_{R',l'}(r_{R'})\, Y_{L'}(\vec{r}_{R'}) S^{0}_{R',L';R,L}. \end{aligned} \tag{2.27}$$

Now, for the solution inside the sphere $\vec{R}$, Eq. 2.23, the radial part $\phi_{R,l}(r,E)$ can be expanded around a fixed and arbitrary energy $E = E_{\nu}(R,l)$,

$$\phi_{R,l}(r,E) \approx \phi_{R,l}(r,E_{\nu}) + (E - E_{\nu})\dot{\phi}_{R,l}(r,E_{\nu}), \tag{2.28}$$

where the dot over ϕ represents the derivative with respect to the energy.

After defining the solutions inside ($\phi_{R,l,\nu}$ and $\dot{\phi}_{R,l,\nu}$) and outside ($K^{\infty}_{R,L}$), there must be a smooth merger of the solutions at the MT sphere contour $r = s$. This is ensured by[3]

$$\chi^{0}_{R,L}(\vec{r}) \approx \frac{\{K^{\infty}, \dot{\phi}_{\nu}\}_{R,l}\phi_{\nu} - \{K^{\infty}, \phi_{\nu}\}_{R,l}\dot{\phi}_{\nu}}{\{\phi_{\nu}, \dot{\phi}_{\nu}\}_{R,l}} \tag{2.29}$$

and where $\{f,g\}_{R,l}$ are the Wronskian determinant $\forall f,g \in [\phi_{\nu}, \dot{\phi}_{\nu}, K^{\infty}]$ at the boundary $r = s$.

2.5.1 Tight-binding and orthogonal representation of the basis

Once the basis are determined by Eq. 2.27 and Eq. 2.28, the electronic structure of the material is obtained by the solution of Eq. 2.18. However, the Hamiltonian matrix is related to the S^0, which has a slow decay with the distance, extending H^0 by several neighbouring shells. For convenience, as going to be discussed later, the Hamiltonian matrix described in terms of a more localized basis allows an efficient use of the recursion method, specially in the treatment of the LMTO-ASA formalism in the real space. This can be achieved by combining two basis representations:

- Orthogonal basis: optimal basis to solve the eigenvalue problem.
- Tight-binding basis: short-ranged Hamiltonian.

For the construction of the canonical base, in the previous section, we first defined a set of envelope functions in order to establish continuity of the basis functions throughout the space. Now the Eq. 2.27 is rewritten as

$$|K\rangle_{\infty} = |K\rangle - |J^0\rangle\, \boldsymbol{S}^0, \tag{2.30}$$

[2] In the basis representations discussion we follow the notation ^{0} for canonical basis, $^-$ tight-binding basis and the absence of index stands for orthogonal basis.

[3] For mathematical construction about boundary conditions, logarithm-derivative and Wronskians see Skriver [45].

here in Dirac notation. Next we performed the augmentation of the envelope functions together with the functions $\phi_{R,L}(r)$ and $\dot{\phi}_{R,L}(r)$ at the sphere boundary, Eq. 2.29. This is a standard procedure to follow in any other LMTO-ASA basis construction.

Next, we consider that the linear combination of $|J^0\rangle$ with a fraction of $|K\rangle$ is also a solution of the Laplace equation,

$$|J^G\rangle = |J^0\rangle - |K\rangle \, \boldsymbol{Q}^G, \tag{2.31}$$

where $\boldsymbol{Q}^G$ is a screening parameter and the superindex G means a general basis. Hence, using Eq. 2.30, a general envelope function can be defined as

$$|K^G\rangle_\infty = |K\rangle - |J^G\rangle \, \boldsymbol{S}^G \tag{2.32}$$

with $\boldsymbol{S}^G$ the screened structure constant matrix [46].

In analogy, we can define a general $\dot{\phi}^G$ by slightly modifying the $\dot{\phi}$ and adding a fraction of ϕ as the following,

$$|\dot{\phi}^G\rangle = |\dot{\phi}\rangle + |\phi\rangle \boldsymbol{o}^G. \tag{2.33}$$

Therefore, the basis, in a general representation, is

$$|\chi^G\rangle_\infty = |\phi\rangle + |\dot{\phi}^G\rangle \boldsymbol{h}^G. \tag{2.34}$$

Note that $\boldsymbol{o}^G$ guarantee a soft augmentation of the radial functions and $\boldsymbol{h}^G$ appears from the boundary conditions at $r = s$.

Subsequently, we can determine the Hamiltonian H^G and the overlap O^G matrices (Eq. 2.19 and Eq. 2.20) in the general basis

$$H^G = {}_\infty\langle\chi^G| - \nabla^2 + V|\chi^G\rangle_\infty = h^G(1 + o^G \, h^G) + E_\nu \, O^G, \tag{2.35}$$

and

$$O^G = {}_\infty\langle\chi^G|\chi^G\rangle_\infty = (1 + o^G \, h^G)(o^G \, h^G + 1). \tag{2.36}$$

where we applied the orthogonal properties between $|\phi\rangle$ and $|\dot{\phi}\rangle$. The terms of order $(h^G + p \, h^G)$, with $p_{R,L} = |\dot{\phi}^2\rangle_{R,L}$, are very small and, therefore, were ignored them in Eq. 2.35 and 2.36. Knowing the Hamiltonian and overlap matrices, the LMTO-ASA eigenvalue equation, in the general basis, is given by

$$(H^G - E \, O^G)u^G = 0. \tag{2.37}$$

In the general basis there is the freedom of choice of the parameter Q^G, tuning the basis localization. The optimal values for Q^G for the tight-binding

parametrization, $\overline{Q}$, have been found empirically [46, 47] and ensure the structure matrix $\overline{S}$ to be short-ranged (until second nearest neighbors), and, consequently, $\overline{H}$. Therefore, the tight-binding equation is

$$(\overline{\boldsymbol{H}} - E\,\overline{\boldsymbol{O}})\,\overline{\boldsymbol{u}} = 0, \tag{2.38}$$

where $^{-}$ stands for tight-binding.

The orthogonal representation turns the eigenvalue equation into particularly simple form, since it orthogonalizes the Hamiltonian matrix. If $o^{G} = o = 0$ in Eq. 2.35 and Eq. 2.36, it follows that the overlap matrix turn the unity matrix $\boldsymbol{O}^{G} = \boldsymbol{O} = \mathbf{1}$. Thus, the orthogonal Hamiltonian is

$$\boldsymbol{H} = \boldsymbol{h} + E_{\nu}. \tag{2.39}$$

Both representations are advantageous, therefore we use the orthogonal form for the Hamiltonian written in terms of parameters from tight-binding representation. First, one can show the relation [45]

$$\boldsymbol{h} = \overline{\boldsymbol{h}}(1 + \overline{\boldsymbol{o}}\overline{\boldsymbol{h}})^{-1}, \tag{2.40}$$

that is valid for a general basis $|\chi^{G}\rangle_{\infty}$, and , here we choose the tight-binding basis. Next, using Eq. 2.40 in Eq. 2.39, we obtain

$$\boldsymbol{H} = E_{\nu} + \overline{\boldsymbol{h}}(\mathbf{1} + \overline{\boldsymbol{o}\,\boldsymbol{h}})^{-1}. \tag{2.41}$$

The term $(\mathbf{1} + \overline{\boldsymbol{o}}\overline{\boldsymbol{h}})^{-1}$ can be expanded in power series around small values of $\overline{\boldsymbol{o}\boldsymbol{h}}$ resulting

$$H = E_{\nu} + \overline{\boldsymbol{h}} - \overline{\boldsymbol{h}\boldsymbol{o}\boldsymbol{h}} + \overline{\boldsymbol{h}\boldsymbol{o}\boldsymbol{h}\boldsymbol{o}\boldsymbol{h}} - \cdots \tag{2.42}$$

The truncation term is chosen in a balance between the numerical precision *versus* computational cost. In general, we consider the two first terms of the Eq. 2.42 as a good approximation to the Hamiltonian.

2.5.2 Potential parameters and Hamiltonian

The matrices $\overline{\boldsymbol{h}}$ and $\overline{\boldsymbol{o}}$ are written in terms of the tight-binding potential parameters $\overline{\boldsymbol{C}}$ and $\overline{\boldsymbol{\Delta}}$, [45]

$$\overline{\boldsymbol{h}} = \overline{\boldsymbol{C}} - E_{\nu} + \overline{\boldsymbol{\Delta}}^{1/2}\,\overline{\boldsymbol{S}}\,\overline{\boldsymbol{\Delta}}^{1/2}, \tag{2.43}$$

where

$$\overline{\boldsymbol{C}} = E_{\nu} - \frac{\{k, \phi\}_{R,l}}{\{k, \overline{\phi}\}_{R,l}}, \tag{2.44}$$

and

$$\overline{\boldsymbol{\Delta}}^{1/2} = \left(\frac{2}{s}\right)^{1/2} \{\bar{j}, \phi\}_{R,l}. \tag{2.45}$$

Also

$$\overline{\boldsymbol{o}} = -\frac{\{\bar{j}, \dot{\phi}\}_{R,l}}{\{\bar{j}, \phi\}_{R,l}}. \tag{2.46}$$

The potential parameters are related to the solution of the Schrödinger-type equation in each sphere R. Thus, it is necessary to use an expression that relates the potential parameters to the tight-binding and orthogonal bases, which is as follows:

$$\frac{\overline{\boldsymbol{\Delta}}^{1/2}}{\boldsymbol{\Delta}^{1/2}} = \frac{\overline{\boldsymbol{C}} - E_\nu}{\boldsymbol{C} - E_\nu}. \tag{2.47}$$

Therefore, the Hamiltonian Eq. 2.42 has a dependence of the (self-consistent) V_R potential by the potential parameters $\overline{C}_{R,l}$ and $\overline{\Delta}_{R,l}$ that represent, respectively, the center and the width of the density of state l from site R. The V_R-independent part is related to the structure matrix $\overline{\boldsymbol{S}}$.

In this thesis, the DFT results of Papers **II**, **III** and **V** were obtained by using the real-space implementation of LMTO in atomic-sphere approximation (RS-LMTO-ASA).

2.6 Real space LMTO-ASA

In order to introduce the RS-LMTO-ASA method, I found the provocative question of V. Heine [48] quite convenient:

> *"Instead of making physics fit the mathematics of perfect periodicity and k space, can we not develop the theory in a way closer and more appropriate to the physics we want to describe?".*

This is really important, if one desire to investigate low symmetry magnetism and understand local effects, apply techniques beyond the constrains of periodicity of Bloch's theorem. For that, the RS-LMTO-ASA method [22, 23, 24] was designed using the powerful electronic structure description of k-space LMTO-ASA with the advantage of solving the eigenvalue problem in real space using the recursion method [48, 49]. The mentioned method is indicated for the study of complex metallic structures, like alloys, defects and impurities in surfaces and other systems that have low symmetry.

2.6.1 Recursion method

In the description of the LMTO-ASA formalism, we have shown that the Hamiltonian in the orthogonal base can be written in terms of tight-binding parameters. However, this is a sparse matrix of dimension $9N \times 9N$, where N is the number of atoms in the cluster and 9 the number of orbitals per atomic site (one s, three p and five d basis functions). Such a dimension of the Hamiltonian matrix requires an efficient inversion of matrices in the process to solve the eigenvalue equation. To overcome this, the recursion method formulated by R. Haydock [48, 49] is introduced.

The purpose of this recursion method is to transform $\boldsymbol{H}$ into a tridiagonal Hamiltonian matrix (Jacobi form) by moving to a new base $\{u_m\}$. After transformation, each $|u_n\rangle$ element should only interact with the previous elements $|u_{n-1}\rangle$ and later $|u_{n+1}\rangle$.

The recursion relation is defined by

$$\boldsymbol{H}|u_n\rangle = a_n|u_n\rangle + b_{n+1}|u_{n+1}\rangle + b_n|u_{n-1}\rangle, \tag{2.48}$$

where $\{a_n, b_n\}$ are the coefficients that describe the interaction of $|u_n\rangle$ with $|u_{n-1}\rangle$ and $|u_{n+1}\rangle$.

To obtain the parameters a_n and b_n, the calculation starts from an arbitrary basis $|u_0\rangle$, related to the atomic site R of interest. Therefore, by imposing the orthonormality of the basis $|u_n\rangle$ and also that $|u_{-1}\rangle = 0$, from Eq. 2.48 for $n = 0$, gives

$$\boldsymbol{H}|u_0\rangle = a_0|u_0\rangle + b_1|u_1\rangle. \tag{2.49}$$

Taken the scalar product with $\langle u_0|$ and using the property of orthogonality, we can determine the coefficient a_0

$$a_0 = \langle u_0|\boldsymbol{H}|u_0\rangle. \tag{2.50}$$

From Eq. 2.49, we get

$$b_1|u_1\rangle = (\boldsymbol{H} - a_0)|u_0\rangle. \tag{2.51}$$

Multiplying Eq. 2.51 by its corresponding dual and using the condition of normalization, we obtain the expression of the coefficient b_1

$$b_1 = [\langle u_0|(\boldsymbol{H} - a_0)^{\dagger}(\boldsymbol{H} - a_0)|u_0\rangle]^{1/2}. \tag{2.52}$$

Once the coefficients are determined, the basis $|u_1\rangle$ turns

$$|u_1\rangle = \frac{(\boldsymbol{H} - a_0)}{b_1}|u_0\rangle. \tag{2.53}$$

Given the values a_0, b_1, $|u_1\rangle$, by the recursion equation we can obtain the a_1, b_2, $|u_2\rangle$ and the other values by analogous form. Therefore, the generalization of the process to obtain the values a_n, b_{n+1}, $|u_{n+1}\rangle$ for any n is:

$$a_n = \langle u_n|\boldsymbol{H}|u_n\rangle, \tag{2.54}$$

$$b_{n+1} = [\langle u_n|(\boldsymbol{H}-a_n)^{\dagger} - \langle u_{n-1}|b_n^*]\ [(\boldsymbol{H}-a_n)|u_n\rangle - b_n|u_{n+1}\rangle]^{1/2}, \quad (2.55)$$

$$|u_{n+1}\rangle = \frac{(\boldsymbol{H}-a_n)|u_n\rangle - b_n|u_{n+1}\rangle}{b_{n+1}}. \quad (2.56)$$

The scalar product of $\langle u_m|$ with Eq. 2.48 defines the elements of the $\boldsymbol{H}$ matrix in the new base

$$H_{m,n} = \langle u_m|\boldsymbol{H}|u_n\rangle = a_n\ \delta_{m,n} + b_{n+1}\ \delta_{m,n+1} + b_n\ \delta_{m,n-1}, \quad (2.57)$$

using the orthonormality property. Finally, the Hamiltonian matrix has the form

$$\boldsymbol{H} = \begin{pmatrix} a_0 & b_1 & 0 & 0 & \cdots \\ b_1 & a_1 & b_2 & 0 & \cdots \\ 0 & b_2 & a_2 & b_3 & \cdots \\ 0 & 0 & b_3 & a_3 & \cdots \\ \vdots & \vdots & \vdots & \vdots & \ddots \end{pmatrix}. \quad (2.58)$$

By this recursion method, the $|u_n\rangle$ orbitals are calculated through various applications of $\boldsymbol{H}$ on the $|u_0\rangle$ orbital. Therefore, as n grows, the $|u_n\rangle$ orbital will extend over a very large region surrounding $n+1$. However, the influence of the $|u_{n+1}\rangle$ over $|u_0\rangle$ is small, so that the inclusion of $|u_{n+1}\rangle$ has no significance for the density of states calculation at site R.

This fact is used as a convergence criterion for the self-consistent calculation, because for a given n the coefficient of $|u_{n+1}\rangle$ will be null, $b_{n+1} = 0$. Nevertheless, for a given cut-off parameter LL, such that $LL < n$, the contributions of $|u_n\rangle$ are already negligible. Therefore, in the RS-LMTO-ASA method, we account coefficients until $n = LL$. This value is chosen according to the size of the cluster and the desired precision.

2.6.2 The Beer-Pettifor terminator

After the processes described in the previous section, we can calculate the local density of states $N(E)$. However, due to the truncation for $LL < n$ we have a discrete density of states (DOS). To obtain the continuous spectrum we calculate the DOS through the properties of the Green functions in the form of a continuous fraction, in addition to using a terminator to simulate the contribution of the terms a_n and b_n related to $n - LL$ terms neglected.

The local density of states (LDOS) for the $|u_0\rangle$ orbital is defined by:

$$N_0(E) = LDOS = -\frac{1}{\pi}\,\mathtt{Im}[G_0(E)], \quad (2.59)$$

where $G_0(E)$ is the first diagonal element of the matrix

$$G_0(E) = \langle u_0|(E-\boldsymbol{H})^{-1}|u_0\rangle, \quad (2.60)$$

with

$$(E-\boldsymbol{H})^{-1} = \begin{pmatrix} (E-a_0) & -b_1 & 0 & 0 & 0 & \cdots \\ -b_1 & (E-a_1) & -b_2 & 0 & 0 & \cdots \\ 0 & -b_2 & (E-a_2) & -b_3 & 0 & \cdots \\ 0 & 0 & -b_3 & (E-a_3) & -b_4 & \cdots \\ \vdots & \vdots & \vdots & \vdots & \vdots & \ddots \end{pmatrix}^{-1} \quad (2.61)$$

The elements of the inverse of $(E-\boldsymbol{H})$ are given by the expression

$$G_0(E) = \frac{D_1(E)}{D_0(E)} \quad (2.62)$$

in which $D_n(E)$ is the determinant of the matrix with the first nth rows and columns suppressed and $D_0(E)$ is the determinant of the matrix $(E-\boldsymbol{H})$.

Given the property of the determinant $D_{i,1}$ of a matrix A with the line i and column 1 suppressed:

$$D_0(E) = \sum_{i=1}^{n} (-1)^{(i+1)} A_{i,1} D_{i,1}\,, \quad (2.63)$$

and then we can write down the determinant $D_0(E)$ as:

$$\begin{aligned} D_0(E) &= (-1)^{(1+1)}(E-a_0)\underbrace{D_{1,1}}_{D_1(E)} + (-1)^{2+1}(-b_1)\underbrace{(-1)^2(-b_1)D_2(E)}_{D_{2,1}} \\ &= (E-a_0)D_1(E) - b_1^2 D_2(E). \end{aligned} \quad (2.64)$$

Substituting Eq. 2.64 into Eq. 2.62 we have

$$\begin{aligned} G_0(E) &= \frac{D_1(E)}{(E-a_0)D_1(E) - b_1^2 D_2(E)} \\ &= \frac{1}{(E-a_0) - b_1^2 \frac{D_2(E)}{D_1(E)}}. \end{aligned} \quad (2.65)$$

After working out the Eq. 2.63, follows

$$\begin{aligned} D_1(E) &= (E-a_1)(-1)^2 D_2(E) - (-b_2)^2 D_3(E) \\ &\vdots \\ D_n(E) &= (E-a_n)D_{n+1}(E) - (-b_{n+1})^2 D_{n+2}(E). \end{aligned} \quad (2.66)$$

If we substitute the Eq. 2.66 in Eq. 2.64, we will have an expression for $G_0(E)$ dependent on a continuous fraction, in the form

$$G_0(E) = \cfrac{1}{(E-a_0) - \cfrac{b_1^2}{(E-a_1) - \cfrac{b_2^2}{(E-a_2) - \cfrac{b_3^2}{\ddots}}}}. \quad (2.67)$$

The Eq. 2.67 may continue indefinitely, resulting in a continuous spectrum, or be truncated at a certain point and generate discrete spectrum. Since we want a continuous spectrum and a reduction of the computational effort, we truncate the fraction in the term LL, and, in order to compensate for the eliminated terms, we use a terminator $t(E)$ to represent them. Thus,

$$G_0(E) = \cfrac{1}{(E-a_0) - \cfrac{b_1^2}{(E-a_1) - \cfrac{b_2^2}{(E-a_2) - \cfrac{b_3^2}{\ddots\ (E-a_{LL-1}) - \cfrac{b_{LL}^2}{(E-a_{LL}) - t(E)}}}}}. \quad (2.68)$$

In this thesis, we use the Beer-Pettifor terminator [50], where $a_n = a$ and $b_n = b$ are constants for $LL < n$ and

$$t(E) = \frac{b^2}{E - a - t(E)}. \quad (2.69)$$

We can manipulate the equation above to obtain the equation of the second degree for $t(E)$

$$t^2(E) - (E-a)\,t(E) + b^2 = 0 \quad (2.70)$$

where the solution is

$$t(E) = \frac{1}{2}\left[(E-a) \pm \sqrt{(E-a-2b)(E-a+2b)}\right]. \quad (2.71)$$

When we replace the Eq. 2.71 in the continuous fraction, it converges to a continuous spectrum for the local density of states in the energy range

$$a - 2b < E < a + 2b. \quad (2.72)$$

Finally, we can calculate the total DOS, summing the densities of state obtained for all the orbitals at a given site.

2.6.3 Self-consistent procedure

The self-consistent calculations within the RS-LMTO-ASA method present different approaches regarding the structure in question. However, all are based in two interconnected self-consistent processes, called the *atomic part* and *main part*. The description of these steps depends on some relationships obtained before.

In the *atomic part*, the potential and potential parameters (C_l, Δ_l and Q_l) are calculated for each non-equivalent site. Thus, the KS equation is solved in the domain of the muffin-tin spheres and equivalent sites are defined as having the

same potential parameters and the other quantities that depend on them, such as occupations, local density of states, etc.

In the *main part*, the eigenvalue problem, Eq. 2.1, is solved using the Hamiltonian as a function of the potential parameters obtained in the previous step. In this way the solutions of the KS equation in the material and the densities of states are calculated.

A summary of the RS-LMTO-ASA self-consistent scheme is presented in the end of this chapter (see Fig. 2.5). In the following is presented a more detailed description of the *atomic* and *main* parts.

Main part

The LMTO-ASA formalism can be written in different base functions $\{\chi_i\}$ [46], so that we can choose the most appropriate for each study. Instead of the canonical basis, in which the LMTO was initially defined, we chose the orthogonal basis, with wave functions orthogonal to each other, and the tight-binding (TB) basis, defined so that interactions between neighboring sites are as small as possible. These bases are related to the canonical basis by a mixture parameter Q (orthogonal basis) or $\overline{Q}$ (TB basis) as discussed before.[4]

Now, considering just the two first terms of Eq. 2.42 and substituting the Eq. 2.43 into it, we find the expression of the self-consistent Hamiltonian used in this thesis,

$$\overline{\boldsymbol{H}} = \overline{\boldsymbol{C}} + \overline{\boldsymbol{\Delta}}^{1/2}\,\overline{\boldsymbol{S}}\,\overline{\boldsymbol{\Delta}}^{1/2}, \tag{2.73}$$

with $\overline{\boldsymbol{S}}$ the structure constant matrix in TB representation given by

$$\overline{\boldsymbol{S}} = \boldsymbol{S}^0(\mathbb{1} - \overline{\boldsymbol{Q}}\boldsymbol{S}^0)^{-1} \tag{2.74}$$

where $\mathbb{1}$ is the identity matrix and $\boldsymbol{S}^0$ is the structure constant in the canonical basis. The $\overline{Q}$ values are known and independent of the material [46]. In the RS-LMTO-ASA method the material's structure remains constant during self-consistency, so the matrix $\overline{\boldsymbol{S}}$ is calculated once and independently of the other steps. Complementary, we calculate the potential parameters related to the band center and the bandwidth in the TB basis, respectively, $\overline{C_l}$ and $\overline{\Delta_l}$ in order to use in Eq. 2.73. These parameters have an initial guess or estimated from the *atomic part* and their values are updated during the self-consistency.

Therefore, we can proceed with the calculation of eigenvalue problem (Eq. 2.1) in the real space, using the recursion method [48, 49] with the help of the Beer and Pettifor's terminator. The recursion method is essential here since the Hamiltonian is a sparse matrix.

Follows the calculation of the local density of states $N_{R,L}(E)$ (LDOS), projected for each non-equivalent site R and orbital $L = \{l, m\}$. Next, using the

[4]The index $^-$ represents the base TB, 0 the canonical basis and the others, without index, the orthogonal basis.

LDOS we can compute the nth order LDOS moment, $m_{R,l}^{(n)}$, given by

$$m_{R,l}^{(n)} = \int_{-\infty}^{E_F} (E - E_{\nu,R,l})^n N_{R,l}(E)\, dE, \tag{2.75}$$

with $E_{\nu,R,l}$ the energy of the center of gravity of the band $L = \{l,m\}$. The integral runs until the Fermi energy (E_F), i.e., the occupied part of the density. Note that for $n = 0$, Eq. 2.75 provides the occupation of each orbital.

Following in the calculations, we must obtain the potential parameters P_l, that determine the boundary conditions for each sphere R, defined as

$$P_l = 0.5 - \frac{1}{\pi}\arctan(D_l), \tag{2.76}$$

with

$$D_l = 1 + (2l+1)\left[\left(\frac{Q_l^{-1}}{2(2l+1)}\,\frac{C_l - E_\nu}{C_l - E_\nu - \Delta Q_l^{-1}}\right) - 1\right]. \tag{2.77}$$

Equation 2.77 is the logarithmic derivative of the KS equation solution for orbital l at the boundary $r = s$ (sphere boundary).

Once the density moments $m_{R,l}^{(n)}$ and the P_l parameters are known, the *atomic part* starts, which when reaches its own self-consistency, return the updated C_l and Δ_l. At this stage, the orthogonal potential parameters are going to be written into TB parameters by

$$\frac{\overline{\boldsymbol{\Delta}}^{1/2}}{\boldsymbol{\Delta}^{1/2}} = \left[\mathbf{1} - (Q - \overline{Q})\,\frac{\boldsymbol{C} - E_\nu}{\boldsymbol{\Delta}}\right] = \frac{\overline{\boldsymbol{C}} - E_\nu}{\boldsymbol{C} - E_\nu}. \tag{2.78}$$

and then update the Hamiltonian by Eq. 2.73. We solve the eigenvalue problem with the recursion method and obtain the new LDOS. Next, the $m_{R,l}^{(n)}$, P_l and E_ν are calculated and the self-consistency is tested. If the difference of the newly calculated moments and of P_l, in relation to those used as input, do not exceeds a threshold, a weighted average between the new and old values of these quantities is taken as input values to the next self-consistent loop. Therefore, the whole procedure is repeated until the self-consistency is reached.

Atomic Part

In this part of the self-consistency, the solution of the KS equation (Eq. 2.5) is solved within each non-equivalent sphere R, according to $m_{R,l}^{(n)}$ and P_l obtained in the *main part*.

Initially, an input guess for $m_{R,l}^{(n)}$ and P_l start the calculation. Thus, the electronic density $\eta_R(r)$ for each non-equivalent sphere R is given by

$$\eta_R(r) = \frac{1}{4\pi}\sum_l \left[m_{R,l}^{(0)}\phi_{R,l}^2 + m_{R,l}^{(2)}(\dot{\phi}_{R,l}^2 + \phi_{R,l}\ddot{\phi}_{R,l})\right], \tag{2.79}$$

where $\dot{\phi}$ and $\ddot{\phi}$ are the first and second derivatives with respect to energy $E = E_\nu$ within the sphere R.

With the value of Eq. 2.79 we calculate the electrostatic potential V_{El} by the Poisson equation

$$\nabla^2 V_{El} = -8\pi\,\eta_R(r), \tag{2.80}$$

here written in atomic units. We also compute the correlation and exchange potential, using $\eta_R(r)$, in the LSDA approximation (Eq. 2.8). Therefore, we determine the potential V_R, as

$$V_R = V_{El}[\eta_R(r)] + V_{xc}[\eta_R(r)] + V_N, \tag{2.81}$$

where $V_N = -\frac{2Z}{r}$.

Given the new potential, Eq. 2.81, and the boundary conditions determined by P_l, we again solve the KS equation to obtain the new ψ_R and calculate the new electronic density $\eta_R(r)$. At this point, the *atomic part* self-consistency test occurs, verifying whether the difference of the new and old electronic densities is sufficiently small for convergence to have been reached. If not self-consistent, a weighted average

$$\eta_R(r) = \beta\,\eta_R^{new}(r) + (1-\beta)\,\eta_R^{old}(r), \tag{2.82}$$

for $0 \leq \beta \leq 1$, is used as an updated density in the calculation of the new V_R, repeating the whole procedure until reaching self-consistency, that is, the value of the difference is smaller than the established value. When self-consistency is reached, the potential parameters (C_l, Δ_l,Q_l) in the orthogonal base are calculated for each non-equivalent site.

The potential V_R, Eq. 2.81, is related with an isolated sphere. In order to correct the potential, by adding the effect of electronic distribution of neighbors sites and self-interaction, we use Madelung potential VES

$$VES_i = \sum_{j\neq i} \frac{2DQ(j)}{|\vec{R}_i - \vec{R}_j|} + \frac{2DQ(i)}{R_{WS}}, \tag{2.83}$$

with $\vec{R}_i$ is the reference sphere, $|\vec{R}_i - \vec{R}_j|$ the distance between the sites i and j, R_{WS} the WS radius and DQ the charge transfer relative to the site i. The first term of Eq. 2.83 represents the potential present in i due to the other sites j, while the second term represents the self-interaction potential. The potential VES will modify the values of the center of the band (parameter C) and the energy of the center of the band E_ν, in the form:

$$C \rightarrow C + VES,$$
$$E_\nu \rightarrow E_\nu + VES.$$

Self-consistent process for metallic surfaces

In the previous session, the generalized self-consistent RS-LMTO-ASA process was described, which can be applied to any metallic system. However, the electrostatic potential VES and the Fermi energy E_F are determined for each type of system studied. That is, there are differences in the computational procedures of the electronic structure for bulk, surface and surface impurities.

For the study of metallic surfaces using this method, the semi-infinite structure of the system is simulated by a cluster with a few thousand atoms whose sites are positioned in atomic planes parallel to crystallographic directions.

In the self-consistent calculation of surfaces, we include the empty spheres (EV-1 and EV-2), which simulate the vacuum region, the metal surface (S) and the metal layers below it (S-1, S-2, S-3, etc.). There will be as many layers as are necessary, so that they all have properties different from the periodic crystalline material. Thus, the layers far from surface or interfaces are going to have its potential parameters fixed to the same ones as in bulk, and they are not modified in the self-consistency. In Fig. 2.2 the described surface scheme is shown.

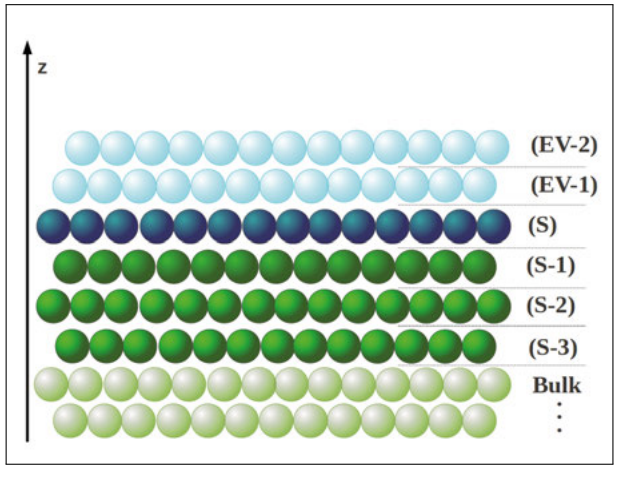

Figure 2.2. Schematic representation of the layers of a generic surface (without defects).

In this semi-infinite configuration, a small amount of charge can be transferred to the regions outside the WS spheres of the most superficial atoms. To simulate this effect, one or two layers of empty WS spheres are included, that is, without electric charge on the principle of self-consistency, in order to simulate the vacuum. During the calculation of the RS-LMTO-ASA the amount of charge in the vicinity of the surface is determined.

This reconfiguration of electrons turns the atomic planes positively charged and the empty spheres negatively charged, as a parallel plate capacitor. This

modifies the electrostatic potential and shift the Fermi level from a constant value proportional to the charge transferred in the surface region [51, 52].

Thus, in the case of systems with two-dimensional symmetry, the Fermi level is fixed at the value found in the self-consistent calculation for the bulk material associated with the semi-infinite part of the studied metal system. In this way, we subtract the potential of all the layers by V_{bulk}.

The Fermi energy (E_F) of the bulk material is obtained by the condition

$$\sum_{R,L} \int_0^{E_F} N_{R,L}(E) dE = \text{valence charge}. \tag{2.84}$$

If the E_F fixed, we can find the LDOS and determine the charge transfer of each site, including the empty spheres.

For periodic crystalline systems VES is obtained by the Ewald's summation, considering the multipolar contributions of the potential plus the charge in each sphere. For the two-dimensional systems, where we have the translational symmetry only along the planes parallel to the surface, each layer has a different electrostatic potential. In this case, charge transfers are used in the two-dimensional Ewald's sum [51, 52], to obtain the Madelung potential and the value of VES at each site.

Self-consistent process for adsorbed atoms on surfaces

The study of nanostructures adsorbed on surfaces using RS-LMTO-ASA requires that previously we have obtained the potential parameters of the specific surface system. Thus, the adsorbed atoms represent a perturbation to the electronic structure of the surface sites next to it. For the simulation we use a surface cluster, with the potential parameters converged, and replace an empty sphere site by an atomic specie of interest, as indicated in Fig. 2.3.

The potential parameters (C and Δ), the charge transfers and the potential VES of the sites away from the defect are fixed at the calculated values for the surface. However, in the region close to the surface impurity, the values of charge transfer ΔQ and potential VES are updated using

$$\Delta Q = \Delta Q_{surf} + \Delta Q_{local} \tag{2.85}$$

and

$$VES = VES_{surf} + VES_{local}, \tag{2.86}$$

in which the indexes $surf$ and $local$ are related, respectively, to the unperturbed and perturbed surfaces sites. Next, the charge added to the system by the adatom is distributed at the first vicinity and the potential VES_{local} will be determined in relation to the resulting charge transfer. Additionally, we use Eq. 2.86 and VES_{surf} to get the new VES for the whole system. In this way, the new potential parameters are combined to the old ones and will be

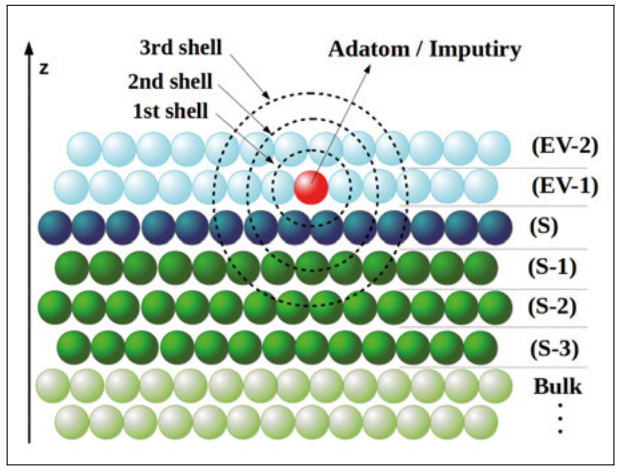

Figure 2.3. Schematic representation of the layers of a surface with an adsorbed atom (adatom). The neighborhood around the adatom is represented by the atoms circumscribed by dotted circles.

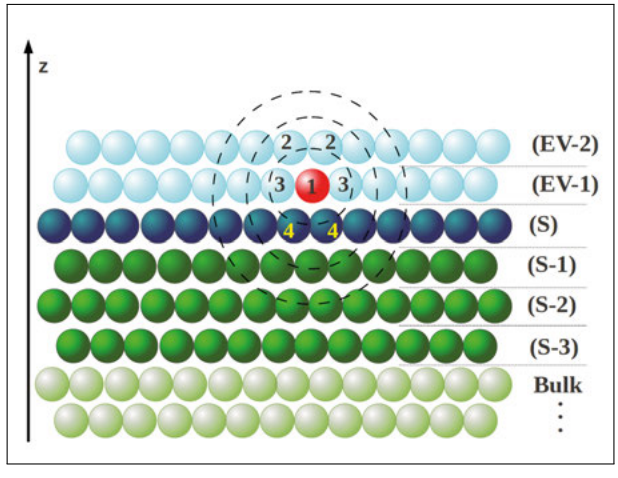

Figure 2.4. Schematic representation of the layers of a surface with an adatom and its inequivalent neighbours, represented by different labels.

used to update the Hamiltonian. Finally, the calculation process continue until obtaining the self-consistency, in a similar process as discussed before.

For a more accurate description of the system, we may also recalculation the potential parameters of sites which are around the impurity, as empty spheres and non-equivalent atoms (see Fig. 2.4). This process of inclusion of neighbors can be extended until a certain neighborhood that no longer is affected by the impurity. Then, in such regions, the potential parameters are similar to those determined for the pure surface.

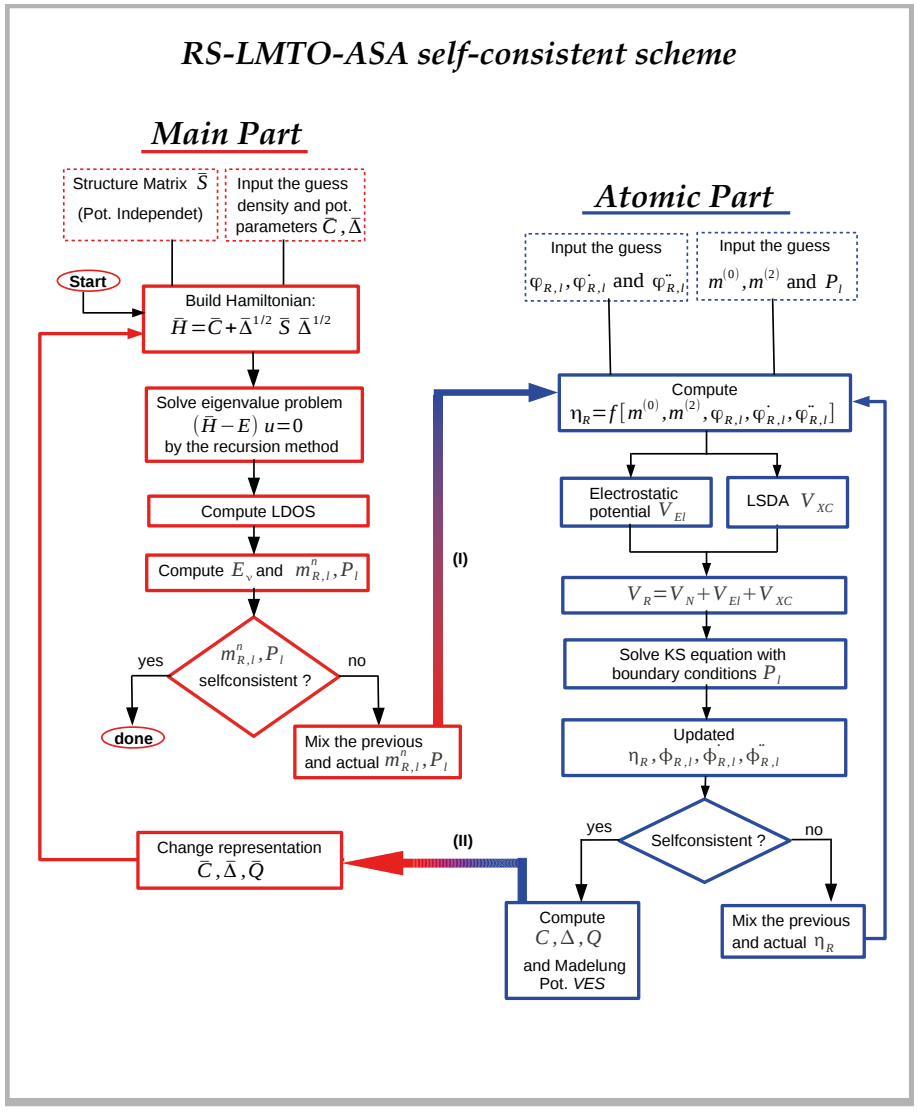

Figure 2.5. RS-LMTO-ASA self-consistent scheme, divided into main part (red) and atomic part (blue). The arrows (I) and (II) indicate the interconnection between them.

3. Magnetic ordering

So far, it was discussed the electron as a quantum mechanical object $\psi_i(\vec{r})$ which obeys the Schrödinger equation or, for practical description of multi-electronic systems, the KS equations. In this chapter, the focus is the magnetism of the electron, which is related to its intrinsic angular momentum – spin, as well the concept of atomic spin and their arrangement in different magnetic textures.

3.1 Band theory of electrons

Apart of the long history of magnetism, the quantum nature of it just break out after the atomic model of Bohr and the discovery of the spin. Thus, the magnetism of the electron, given by its total magnetic moment m_e, is divided into orbital (m_o) and spin (m_s) contributions as

$$m_o^e = -\frac{\mu_B}{\hbar}\langle \mathbf{l} \rangle \tag{3.1}$$

$$m_s^e = -g_s \frac{\mu_B}{\hbar}\langle \mathbf{s} \rangle \tag{3.2}$$

$$m^e = (2s+l)\frac{\mu_B}{\hbar} \tag{3.3}$$

where $\langle\ \rangle$ stands for the expected value of the angular momentum $\mathbf{l}$ and spin $\mathbf{s}$ operators, g_s the gyromagnetic factor and $\mu_B = \frac{e\hbar}{2m_e}$ is the Bohr magneton. Therefore, the magnetism of multi-electronic atom is deeply related with its ground state configuration and is given by the Hund's rules [53].

The electron in a crystal is subjected to a l dependent potential and leads the valence electron localization or delocalization, accordingly to its orbital characteristic [54]. In addition, the electrons form bonded states (overlap) and may hop from site to site.

In the solid state, the magnetism of localized electrons is described with a certain accuracy by Hund's rules, while the ones weakly connected to the nuclei usually have noninteger magnetic moment (in μ_B units). Therefore, the itinerant magnetism is associated with delocalized electrons and require a specific approach by the band theory.

In this picture, the electrons fill the possible delocalized states until the Fermi energy, forming majority and minority electron spin bands, as in Fig. 3.1.

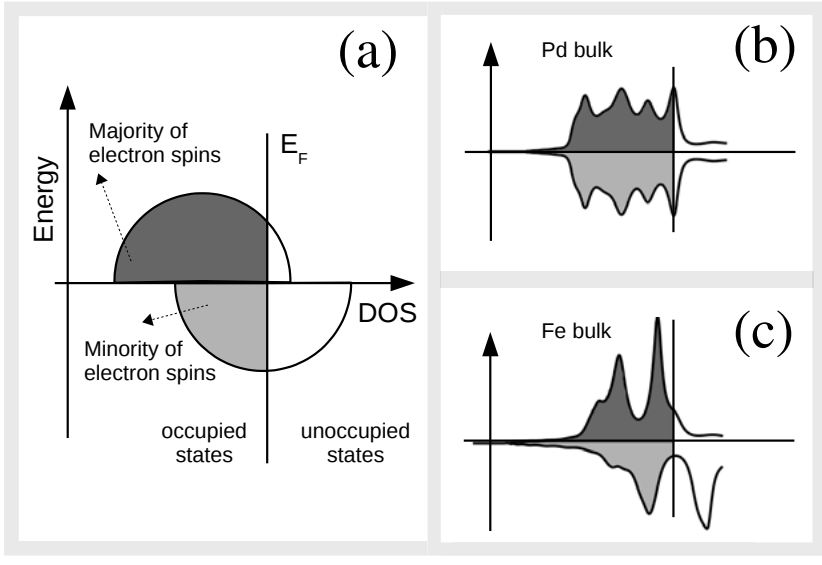

Figure 3.1. Density of states (DOS) of a transition metal with the occupied electron states below the Fermi energy (E_F) represented by filled curves (a). If the majority and minority bands are equally occupied, follows $m = 0$, as for fcc Pd (b). If the bands are unequally occupied, $m \neq 0$, as for bcc Fe (c).

The density of states, expressed as Eq. 2.75, for $n = 0$, represents the density of electron energy levels and is strongly dependent on the crystal structure and chemical environment. From the LDOS, the spin magnetic moment is given by,

$$m_s = \mu_B(DOS^{\uparrow} - DOS^{\downarrow}). \tag{3.4}$$

Thus, in the ground state, a paramagnetic material has equally occupied majority and minority bands below the E_F, Fig. 3.1.b, while a magnetic one has unequally occupied the bands due to the exchange-splitting.

3.2 Magnetic ordering

The magnetic material could present spontaneous magnetic ordering, as the later 3*d* transition metals. Therefore, if exists a global axis of magnetization, the spins could be aligned parallel (ferromagnetic) or antiparallel (antiferromagnetic) with each other, as shown in Fig 3.2. In the case of antiferromagnetic (AFM) materials, if the antiparallel magnetic moments have different size, it is called ferrimagnetic (FI).

The band theory of magnetism, by the Stoner criteria [55], describe that the transition from the paramagnetic to a FM phase will occur if a determined material exhibits a high density of states at the Fermi level. Thus, for pure crystalline systems (bulk), the ferromagnetism is associated with elements at the end of the 3d series, i.e., bcc Fe, hcp Co and fcc Ni. For other elements the minimum energy is related to the AFM phase, mainly for materials with semi-filled bands as in the case of Cr and Mn bulk.

In cases that more than one quantization axis exist, the magnetic ordering is denominated non-collinear. This magnetic ordering give rise to complex spin textures such as spins spiral [56] and skyrmions [57, 58, 59]. The non-collinear magnetic textures are observed with the SP-STM technique, in which the STM tip is magnetized in a given direction, giving a magnetic contrast to the scanned image.

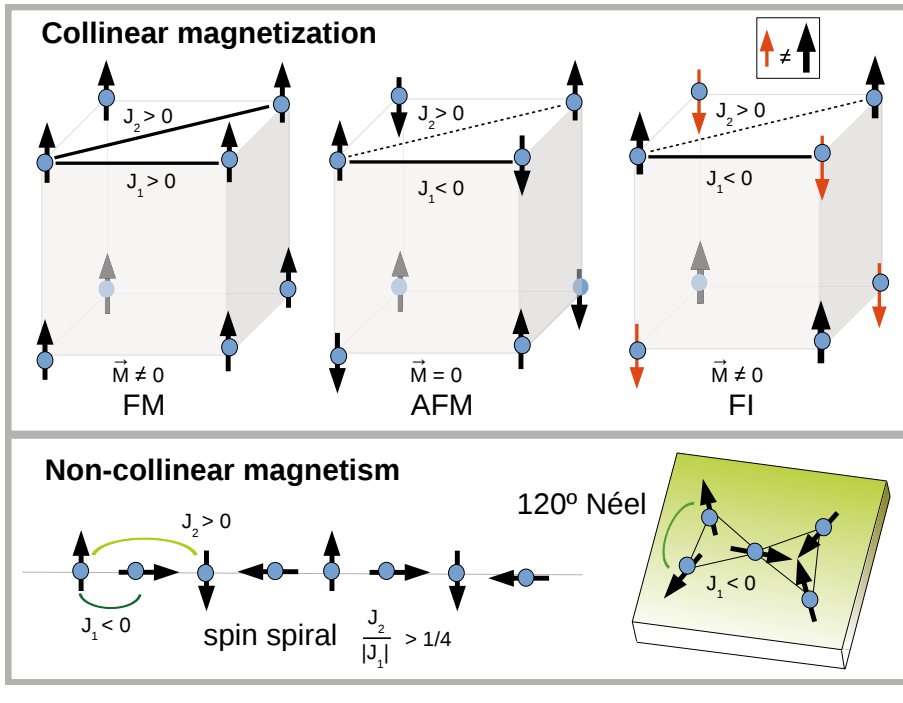

Figure 3.2. The magnetic ordering as collinear (upper panel) and non-collinear (bottom panel). The J_1 and J_2 are the exchange coupling J_{ij} between first and second neighbors, repectively.

Regarding the DFT treatment of non-collinear magnetism, there are several theoretical-computational methods that treat it in case of periodic systems. However, few methods are capable of investigate non-collinear magnetism in nanostructured materials with low symmetry, see [24, 60]. In the LSDA was shown that the electron density is expressed by the density matrix $\boldsymbol{\rho}(\vec{r})$, Eq.

2.9, which is divided into a nonmagnetic electron density term $n(\vec{r})$ and another of the electronic density of magnetization $\boldsymbol{m}(\vec{r})$.

By the recurrence method, the LDOS can be obtained by the following equation

$$N(E) = -\frac{1}{\pi} \text{Im } Tr[\boldsymbol{G}(E)], \tag{3.5}$$

when $\boldsymbol{G}(E)$ is the matrix whose elements are Green functions given by

$$\boldsymbol{G}(E) = (E - \boldsymbol{H})^{-1}, \tag{3.6}$$

for each atomic sphere centered in R and orbital l.

Similarly, the magnetic density of states, applied for a collinear arrangement, is calculated as

$$m(E) = -\frac{1}{\pi} \text{Im } Tr[\sigma_z G(E)], \tag{3.7}$$

with the preferential quantization axis been the z-axis, represented in Eq. 3.7 by the Pauli matrix σ_z, resulting in magnetization $m_z(E)$.

To deal with non-collinear magnetism it is needed to calculate the terms outside the main diagonal of Eq. 3.6. For that, the recurrence method has a high computational cost. However we can use successive unit transformations $\mathscr{U}$ to Hamiltonian $H \to H' = \mathscr{U} H \mathscr{U}^\dagger$, which can be extended to Green functions $G' = \mathscr{U} G \mathscr{U}^\dagger$ [24]. In this way, the generalized magnetic state density is obtained, including the possibility of non-collinear arrangement,

$$m(E) = -\frac{1}{\pi} \text{Im } Tr[\boldsymbol{\sigma}' \boldsymbol{G}'(E)], \tag{3.8}$$

with $\boldsymbol{\sigma}'$ and $\boldsymbol{G}'$, respectively, a Pauli matrix and the Green function after the chosen unit transformation. This corresponds to a spin rotation where the transformation matrix $\mathscr{U}$ can be calculated using the rotation matrices for spin-$1/2$, so that

$$\mathscr{U} \sigma_j \mathscr{U}^\dagger = \sigma_z' \ \ (j = x, y, z). \tag{3.9}$$

However, $\mathscr{U}$ is defined differently for each direction, so that each of the transformations represented by Eq. 3.9 results in a diagonal matrix. This means that by rotating $\boldsymbol{\sigma}$ to a $\boldsymbol{\sigma}'$, we will do it so that σ_x' is a diagonal matrix and consequently we can find the $m_x(E)$ from Eq. 3.8. In analogy, we can find the component $m_y(E)$ from σ_y', also diagonal.

By decomposing Hamiltonian into a spin dependent part ($\boldsymbol{b}$) and another independent of this (H^0), the unit transformation $\mathscr{U}$ only acts on the first. In this way

$$\boldsymbol{H}' = H^0 \mathbb{1} + \boldsymbol{b} \cdot \mathscr{U} \boldsymbol{\sigma} \mathscr{U}^\dagger. \tag{3.10}$$

Then, the elements of Eq. 3.10 are constructed using LMTO parameters in the tight-binding base and the first-order approximation in energy. Therefore, the independent part of the spin is given by

$$H^0_{Q,Q'} = \overline{C}^0_Q + \overline{\Delta}^{0\,1/2}_Q \overline{S}_{Q,Q'} \overline{\Delta}^{0\,1/2}_{Q'} + \overline{\Delta}^{1\,1/2}_Q \overline{S}_{Q,Q'} \overline{\Delta}^{1\,1/2}_{Q'} \boldsymbol{m}_Q \cdot \boldsymbol{m}_{Q'}, \quad (3.11)$$

while the independent part is

$$\begin{aligned} \boldsymbol{b}_{Q,Q'} = & \left(\overline{C}^1_Q + \overline{\Delta}^{1\,1/2}_Q \overline{S}_{Q,Q'} \overline{\Delta}^{0\,1/2}_{Q'} \right) \boldsymbol{m}_Q + \overline{\Delta}^{0\,1/2}_Q \overline{S}_{Q,Q'} \overline{\Delta}^{1\,1/2}_{Q'} \boldsymbol{m}_{Q'} + \\ & + \overline{\Delta}^{1\,1/2}_Q \overline{S}_{Q,Q'} \overline{\Delta}^{1\,1/2}_{Q'} \boldsymbol{m}_Q \times \boldsymbol{m}_{Q'}, \end{aligned} \quad (3.12)$$

where $Q = R, L$ and the indices 0 and 1 denote independent and spin-dependent potential parameters, respectively.

The Hamiltonian in Eq. 3.10 is solved by the recurrence method three times, once a unit transformation is made for each direction. At the end we obtain $m_x(E)$, $m_y(E)$ and $m_z(E)$, that integrated up to the Fermi level correspond to the direction of the local spin moment.

3.3 Heisenberg Hamiltonian and exchange coupling

Under certain conditions, a classical effective spin Hamiltonian is adequate for the description of the spin fluctuations of the itinerant electrons. Therefore,

$$\mathscr{H}_{Hei} = -\sum_{i \neq j} J_{ij}\, \hat{\mathbf{s}}_i \cdot \hat{\mathbf{s}}_j, \quad (3.13)$$

known as the Heisenberg Hamiltonian, with $\hat{\mathbf{s}}_i$ the unit vector that indicates the direction of the magnetic moment at the site i and J_{ij} the exchange parameter between the moments $\boldsymbol{s}_i$ and $\boldsymbol{s}_j$. Though the Heisenberg model was designed for systems in which the moments are localized, it is suitable for metals with sufficiently larger m_s. Consequently, in case the atomic spins are parallel (FM), the minimum energy according to Eq. 3.13 is related to $J_{ij} > 0$. Complementary, in case of anti-parallel spins (AFM), follows that $J_{ij} < 0$ (see Fig. 3.2 and 3.3).

Regarding to non-collinear magnetic configurations, for example $\nearrow\nwarrow$ and $\nwarrow\nearrow$, have the same energy according to Eq. 3.13, if the angle between the moments are equal. Thus, the Heisenberg exchange interaction is also called symmetric exchange interaction.

3.3.1 Heisenberg exchange and LKAG formula

The J_{ij} usually is obtained experimentally by fitting inelastic neutron scattering data to the Heisenberg Hamiltonian. From the electronic structure calculations, one can estimate theoretically the J_{ij} using the formulation of Liechtenstein-Katsnelson-Antropov-Gubanov (LKAG) [61]. This method associate the J_{ij}

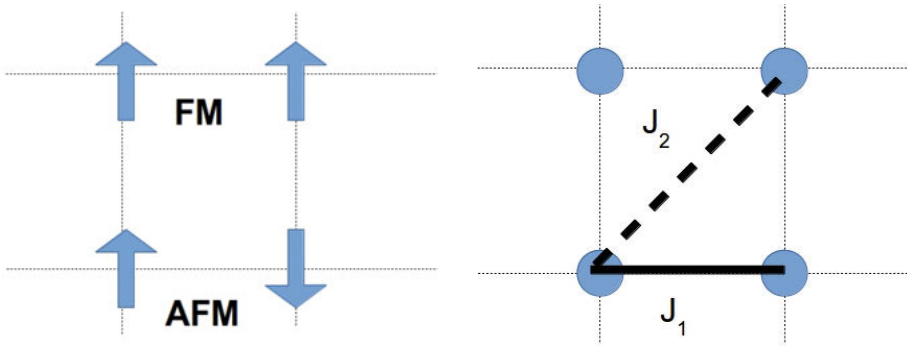

Figure 3.3. The FM and AFM ordering (left). The Heisenberg model considering atoms the distance of first J_1 and second neighbors J_2 in a square lattice (right).

to the energy variation related to an infinitesimal two-site-rotation of the moments at the sites i and j, by means of the force theorem.

In this thesis, the calculation of exchange interaction has a similar approach, computing the J_{ij}'s using the Green functions [62] instead of the scattering path operator formalism. Using the relations between the true and auxiliary Green's functions in the orthogonal representation of the LMTO-ASA, where the second derivative of the potential function is zero, follows that

$$J_{ij} = \frac{1}{4\pi} \text{ Im } Tr \left(\int_{-\infty}^{E_F} \delta_i(E) G_{ij}^{\uparrow\uparrow} \delta_j(E) G_{ji}^{\downarrow\downarrow} dE \right), \tag{3.14}$$

with trace (Tr) over orbital indices $l = 0, 1, 2$, $G_{ij}^{\sigma\sigma}$ is the electron propagator between i and j sites, and $\delta_{l,i}$ a diagonal matrix with elements

$$\delta_{l,i}(E) = \frac{C_{l,i}^{\downarrow}\Delta_{l,i}^{\uparrow} - C_{l,i}^{\uparrow}\Delta_{l,i}^{\downarrow} + (\Delta_{l,i}^{\downarrow} - \Delta_{l,i}^{\uparrow})E}{(\Delta_{l,i}^{\uparrow}\Delta_{l,i}^{\downarrow})^{1/2}} \tag{3.15}$$

where $C_{l,i}^{\sigma}$ and $\Delta_{l,i}^{\sigma}$ are the potential parameters of the site i in the orthogonal basis. If $\Delta_{l,i}^{\downarrow} = \Delta_{l,i}^{\uparrow}$, Eq. 3.15 becomes independent of energy, depending only on the difference between the spin-up and spin-down bands center, as consequence.

3.3.2 Exchange interaction in the non-collinear magnetism

The calculation of exchange parameters can be extended in order to compute the exchange coupling for non-collinear spin configurations[28]. In the context of the multiple scattering theory it is possible to define the matrix $A^{\alpha\beta}$

$$A^{\alpha\beta} = \frac{1}{\pi} \int_{-\infty}^{E_F} dE \ \texttt{Im}Tr(p_i T_{ij}^{\alpha} p_j T_{ji}^{\beta}), \tag{3.16}$$

with $\alpha,\beta = 0,x,y,z$, p_i is related to the magnetic part of the single site scattering operator and T_{ij} with the scattering path operator.

To the extent that there is a global quantization axis, a choice of coordinates can be made so that T_{ij} has only the z-component as non-zero contribution between two sites. This implies that $A^{\alpha\beta} \rightarrow (A^{00}, A^{zz}) \neq 0$. Thus, at the collinear boundary Eq. 3.16 turns

$$J_{col} = A^{00} - A^{zz} = \frac{1}{\pi}\int_{-\infty}^{E_F} dE \; \mathtt{Im}Tr(p_i T_{ij}^{\uparrow} p_j T_{ji}^{\downarrow}) \tag{3.17}$$

where $T^{\uparrow} = T_{ij}^{0} + T_{ij}^{z}$ and $T^{\downarrow} = T_{ij}^{0} - T_{ij}^{z}$. The Eq. 3.17 recovers the result of LKAG formalism. Thus, the collinear exchange parameters are A^{00} and A^{zz}, been the rest responsible for non-collinear part. Therefore, the exchange coupling when there is a non-collinear spins configuration is defined as

$$J_{noncol} = A^{00} - A^{xx} - A^{yy} - A^{zz}. \tag{3.18}$$

The connection between the formalisms of the multiple scattering theory and the LMTO-ASA is made according to Ref. [63]. In this case, the Eq. 3.16 can be applied for the calculation of the J_{noncol} by making the substitutions $p = \frac{(\bar{C}-E_\nu)}{\bar{\Delta}}$ and $T = \bar{\Delta}^{1/2} G \bar{\Delta}^{1/2}$. In Paper **III** this formalism is applied.

3.4 The Dzyaloshinskii-Moriya interaction

One of the interactions responsible for non-collinear magnetization is the interaction described by Dzyaloshinsky [64] and Moriya [65](DM) due to the spin-orbit coupling and the translation symmetry of the crystalline lattice. The spin Hamiltonian model of this interaction is

$$\mathscr{H}_{DM} = \sum_{i \neq j} \mathbf{D}_{ij} \, \hat{\mathbf{s}}_i \times \hat{\mathbf{s}}_j \tag{3.19}$$

with $\mathbf{D}_{ij}$ is known as the Dzyaloshinsky-Moriya vector. Thus, the DMI is a non-symmetric interaction and distinguish the energy associated with $\nearrow\nwarrow$ and $\nwarrow\nearrow$ according to Eq. 3.19, differently from the Heisenberg exchange interaction. Depending on the symmetry of the material, the magnetization can be complex and characterized by the chirality $\vec{C} = \hat{\mathbf{s}}_i \times \hat{\mathbf{s}}_j$, that represents the sense of handiness of the magnetization. For example, spin-spirals [56] and skyrmions [57, 59] due to DMI.

There are some approaches of calculating the direction of $\mathbf{D}_{ij}$ vector, either by the micromagnetic method [66], the Force Theorem [67] or even by rules of symmetry [65, 68]. In the RS-LMTO-ASA, the DM interaction is present when we consider the spin-orbit coupling in the self-consistent calculations, however it is not possible yet to extract direct from the potential parameters the direction and modulus of the DM in the same way as it is performed to the J_{ij}.

3.5 Magnetocrystalline anisotropy

From early experiments, the magnetic anisotropy can be measured, for example, comparing the hysteresis loop of two materials. In Fig. 3.4.a can be seen that the *hard* material demands higher fields than the *soft* one in order to reverse its magnetization. Additionally, Fig. 3.4.b, illustrates that an material might have a “square" or “narrow" hysteresis loop depending the angle θ of the field with respect to some specific magnetization direction $\{\hat{e}_x, \hat{e}_y, \hat{e}_z\}$ (that may or may not correspond to $\{\vec{a}_1, \vec{a}_2, \vec{a}_3\}$ crystallographic axis). Therefore, it reveals an *easy-axis* (or preferential axis) that the magnetic moments of a magnet tend to be aligned with.

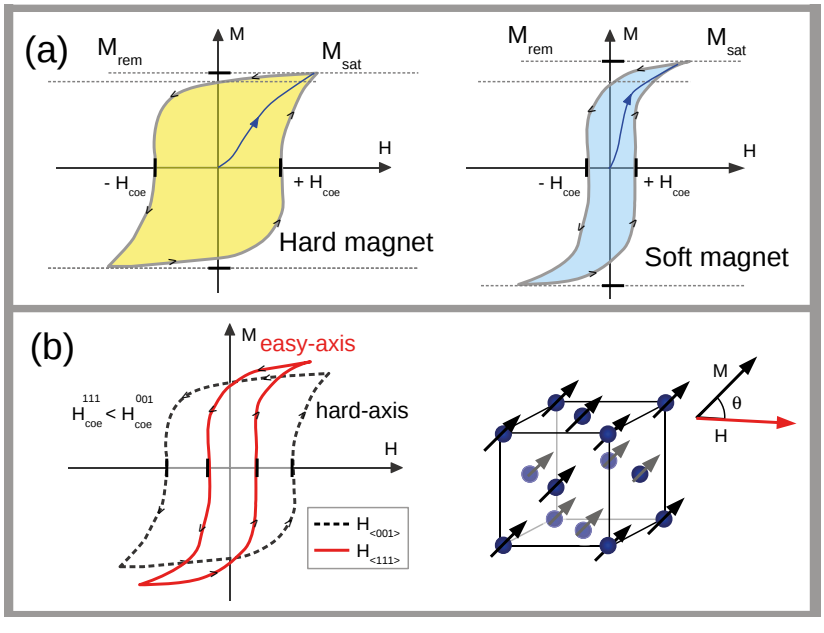

Figure 3.4. The hysteresis loop of (a) a hard (left) and soft (right) ferromagnet. As soon the field $\vec{H}$ is applied, the virgin curve (blue) shows the increase of the magnetization until reach the saturation magnetization M_{sat}. After reverse the field, the magnetization assumes its remanent magnetization M_{rem} at $\vec{H} = 0$. The coercive field H_{coe} is the reverse field needed to reduce the magnetization to zero. (b) Different hysteresis loop depending on the angle θ between the field and magnetization.

The energy associated with the *magnetic anisotropy* energy (MAE) can be modeled by

$$E_{MAE}^{uni} = K_1 \sin^2(\theta) + K_2 \sin^4(\theta) + K_2 \sin^6(\theta) \tag{3.20}$$

with θ the polar angle. The expression above contains the first, second and third order of uniaxial anisotropy and the respective anisotropy constants K_1, K_2 and K_3. According to the sign of the anisotropy constants K the Eq.3.20

represents the easy-axis, easy-plane or easy-cone anisotropy. The MAE is intimately related to electrostatic crystal-field or spin-orbit coupling [69]. Thus, in order to compute the K_1, one may extract this information from the electronic structure of the magnetic material by total energy calculations, force theorem method, torque method or Bruno's formula [70].

In case of 3d transition metals, most of the anisotropic energy is attributed to spin-orbit effects [69]. An approach is to consider the spin-orbit term via perturbation theory and, in an uniaxial magnet, the first non-zero contribution appears from second-order perturbation

$$\mathscr{H}_{soc} = \xi^2 \sum_n \sum_m \frac{|\langle \psi_n | \mathbf{L} \cdot \mathbf{S} | \psi_m \rangle|^2}{E_n - E_m} \tag{3.21}$$

with E_n and E_m the eigenvalues of the wave-function $|\psi_n\rangle$ and $|\psi_m\rangle$ related to the unperturbed Hamiltonian. Considering that n and m are, respectively, occupied and unoccupied states, there must be cases in which the states across the Fermi energy are selectively enhancing the expected value $\langle \psi_n | \mathbf{L} \cdot \mathbf{S} | \psi_m \rangle$. Thereby, Eq.3.21 shows that even if ξ is small the MAE can be significant.

An alternative procedure to compute MAE is to use the orbital moment anisotropy ΔL, via Bruno's formula [70, 71, 72],

$$E_{\mathrm{MAE}} = -\frac{\xi}{4\mu_B} \Delta L \tag{3.22}$$

with $\Delta L = L_{\hat{\mathbf{n}}_1} - L_{\hat{\mathbf{n}}_2}$ the difference of the orbital moment projection L for two different global quantization axes, $\hat{n}_1$ and $\hat{n}_2$

For Fe, Co and Ni the orbital moment is a result of the SOC [73]. In addition, the majority spin band is essentially filled and only minority spin states contribute to the density of states at the Fermi energy. For that, the spin diagonal matrix elements of the spin orbit coupling should dominate the contribution to the MAE [74]. When minority spin states dominate the MAE, the easy axis is parallel to the direction of maximum orbital magnetic moment. In this thesis the Bruno's formula was used to compute the local magnetic anisotropy in Paper **II**.

4. Magnetization dynamics

The investigation of magnetic moments and their interaction of magnetic fields is an important access to the magnetism of materials. The atomic magnetic moment can be seen as a magnetic dipole $\vec{m}$ on the atomic scale. Hence, in the presence of an external magnetic field $\vec{H}_{ext}$, the torque that $\vec{m}$ experiences is given by

$$\vec{T} = \vec{m} \times \vec{H}_{ext}. \tag{4.1}$$

Using the classical relation between the torque and angular momentum $\frac{d\vec{L}}{dt} = \vec{T}$, and that the $\vec{m}$ is proportional to $\vec{L}$ by the gyromagnetic ratio γ, $\vec{m} = \gamma\vec{L}$, follows from Eq.4.1,

$$\frac{d\vec{m}}{dt} = \gamma \left[\vec{m} \times \vec{H}_{ext}\right]. \tag{4.2}$$

Equation 4.2 is the equation of motion of a magnetic moment in the field $\vec{H}$.

Experimentally it is known that the magnetization eventually moves toward the field direction. Therefore, an additional dissipative torque $\vec{T}_{dis}$ must be considered and it is defined by

$$\vec{T}_{dis} \sim \left[\vec{m} \times \frac{d\vec{m}}{dt}\right]. \tag{4.3}$$

In order to ensure the rotation in direction to the z-axis, $\vec{T}_{dis}$ in Eq. 4.3 is perpendicular to the precessional torque and magnetic moment. From Eq. 4.2 and Eq. 4.3, follows

$$\frac{d\vec{m}}{dt} = \gamma \left[\vec{m} \times \vec{H}_{ext}\right] + \frac{\alpha\gamma}{m} \left[\vec{m} \times \left(\vec{m} \times \vec{H}_{ext}\right)\right], \tag{4.4}$$

where $m = |\vec{m}|$ and α denotes the dimensionless damping parameter, which contributes to the dissipation of energy. The Eq. 4.4 is the Landau-Lifshitz equation of motion for the magnetization. The relationship of the $\vec{B}_{eff}$ and damping torque are illustrated in Fig. 4.1.

4.1 Landau-Lifshitz-Gilbert equation

In the Gilbert representation of the LL equation, the Eq. 4.4 is slightly modified to

$$(1+\alpha^2)\,\frac{d\vec{m}}{dt} = \gamma \left[\vec{m} \times \vec{H}_{ext}\right] + \frac{\alpha\gamma}{m} \left[\vec{m} \times \left(\vec{m} \times \vec{H}_{ext}\right)\right], \tag{4.5}$$

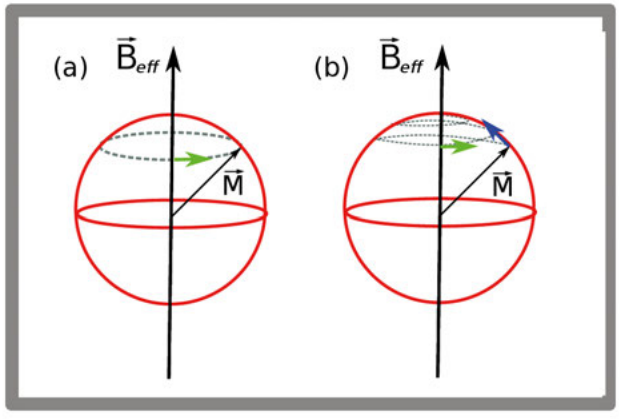

Figure 4.1. Schematic representation of magnetic moment under the influence of magnetic field only with the precession (a) and both precession and damping (b). The green arrow indicates the precession and blue the damping.

where a damping term which depends on the time derivative of the magnetization was added, this equation is known as the Landau-Lifshitz-Gilbert (LLG) equation. In case α is small, the α^2 term is negligible and we recover the LL equation.

It is possible to work with Eq. 4.5 in order to be mathematically equivalent to Eq. 4.4,

$$\frac{d\vec{m}}{dt} = \gamma' \left[\vec{m} \times \vec{H}_{ext}\right] + \frac{\alpha'}{m} \left[\vec{m} \times \left(\vec{m} \times \vec{H}_{ext}\right)\right], \tag{4.6}$$

which is achieved if $\gamma' = \frac{\gamma}{1+\alpha^2}$ and $\alpha' = \frac{\gamma\alpha}{1+\alpha^2}$.

4.2 Atomistic spin dynamics

The energy associated to the atomic spins interactions is described by the Heisenberg Hamiltonian, as discussed previously. From Eq. 3.13, follows

$$\begin{aligned} \mathscr{H}_{Hei} &= -\underbrace{\left[\frac{1}{2}\sum_{i\neq j} J_{ij}\,\vec{m}_i\right]}_{\vec{B}_{eff}} \cdot \vec{m}_j \\ \mathscr{H}_{Hei} &= -\vec{B}_{eff} \cdot \vec{m}_j \end{aligned} \tag{4.7}$$

where $\vec{B}_{eff}$ is called the effective field, since the Eq.4.7 has the same form of the energy of a magnetic dipole $\vec{m}$ in a magnetic field $E = -\vec{m} \cdot \vec{H}_{ext}$. Hence,

the Eq.4.7 has the physical meaning that an atomic moment $\vec{m}_j$ is subject to an effective field produced by all $\vec{m}_i$ in the neighbourhood.

In some cases other magnetic interactions than exclusively exchange interaction may be present in a crystal, as anti-symmetric interatomic exchange coupling (Dzyaloshinski-Moriya), magnetocrystalline anisotropy, dipole interactions and Zeeman terms. For that, one can consider a extended Hamiltonian collecting all relevant interactions in an electronic system, such as symmetric and antisymmetric terms

$$\mathscr{H} = -\frac{1}{2}\sum_{i\neq j} J_{ij}\,\vec{m}_i \cdot \vec{m}_j + \sum_{i\neq j} \vec{D}_{ij}\,\vec{m}_i \times \vec{m}_j + \ldots \tag{4.8}$$

In this context, the definition of effective field $\vec{B}_{eff}$ is generalized to

$$\vec{B}_{eff} = -\frac{\partial \mathscr{H}}{\partial \vec{m}_j} \tag{4.9}$$

and the LLG equation, Eq. 4.6, is rewritten as

$$\frac{d\vec{m}_i}{dt} = \gamma' \left[\vec{m}_i \times \vec{B}_{eff}\right] + \frac{\alpha'}{m}\left[\vec{m}_i \times \left(\vec{m}_i \times \vec{B}_{eff}\right)\right]. \tag{4.10}$$

The Eq. 4.10 is the atomistic version of LLG equation and represents the equation of motion for an atomic moment $\vec{m}_i$ subject to the effective field produced by its neighbouring atomic moments in a crystal.

4.2.1 Temperature effects

It is noticed experimentally that the magnetic moments tend to align themselves in a direction parallel to the magnetic field, however, the temperature tends to dismantle the alignment. The motion of $\vec{m}$ in finite-temperature is modeled by the Langevin dynamics, in which the temperature is included in the system by a stochastic field $\vec{b}_i$. Then, it is possible to rewrite the effective field as

$$\vec{B}_{eff} = \vec{B}_{eff} + \vec{b}_i, \tag{4.11}$$

resulting in a stochastic LLG equation given by,

$$\frac{d\vec{m}_i}{dt} = -\gamma\,\vec{m}_i \times [\vec{B}_i + \vec{b}_i(t)] - \gamma\,\frac{\alpha}{m_i}\,\vec{m}_i \times (\vec{m}_i \times \{\vec{B}_i + \vec{b}_i(t)]\}, \tag{4.12}$$

with the thermal fluctuations represented by the stochastic magnetics field $\vec{b}_i$. The Gilbert damping constant α, which contributes to the dissipation of energy, assist the system to lead the thermal equilibrium.

The stochastic fields are represented by fluctuating fields with a Gaussian white noise shape. Therefore, $\vec{b}_i$ accounts with the properties of being uncorrelated in space and time. This is expressed by the criteria

$$\langle \vec{b}_i(t) \rangle = 0, \tag{4.13}$$

which states that the time average of the stochastic field is zero, and

$$\langle \vec{b}_\mu(t) \vec{b}_\nu(t') \rangle = 2D\delta_{\mu\nu}\delta(t-t') \tag{4.14}$$

with

$$D = \frac{\alpha}{1+\alpha^2} \frac{k_B T}{\mu_B m} \tag{4.15}$$

where the Dirac delta $\delta(t-t')$ states that the stochastic field is uncorrelated in time, while the Kronecker delta $\delta_{\mu\nu}$, with $\{\mu, \nu\}$ representing spatial coordinates, states that the field $\vec{b}$ is the uncorrelated in space. The relation of the stochastic field and temperature T is represented in Eq. 4.15, called the fluctuation strength [26]. The relation of D with the energy dissipation comes from the main statement of the fluctuation dissipation theorem [75, 76].

Lastly, solving Eq. 4.12 means having access to the dynamics of each atomic magnetic moment $\vec{m}_i(t)$ in a solid, known as Atomistic Spin Dynamics (ASD) [77, 26]. Thus, in this thesis the ASD simulations were computed using the Uppsala Atomistic Spin Dynamics (UppASD) computational package [78]. In the simulations, the numerical method used to solve the stochastic differential equation Eq. 4.12 was the Semi-implicit Midpoint Solver [79], with time increments of typically $\Delta t = 0.1$ femtoseconds, i.e., 10^{-16} seconds.

Monte Carlo method

Some static properties as critical temperature, magnetic susceptibility or heat capacity can be obtained in a efficient manner using Monte Carlo (MC) methods instead of using the LLG equation, Eq. 4.12.

The MC methods are a collection of sampling algorithms dedicated to search through the possible configurations of a system. The main goal is to select the most probable configuration that comply with given conditions. In the context of magnetism, the Metropolis algorithm is used to describe the static properties of a magnetic system, given that the energy is represented by a spin Hamiltonian.

The configurations are selected from a previous state using a transition probability which depends on the energy difference $\Delta E = E_{intial} - E_{final}$ between the initial and final states. The final state is generated according to a Markov chain of states, which means that each new state is generated directly from the preceding state.

Given an initial magnetic arrangement for the system, the Metropolis algorithm can be described as follows:

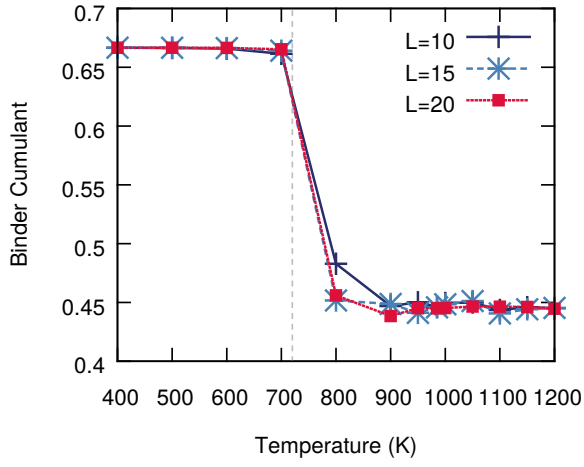

Figure 4.2. Example of the scaling method using the Binder cumulant U_4.

1. Choose a site i
2. Calculate the energy change ΔE if the spin at site i is rotated
3. Generate a random number *rand* such that $0 < rand < 1$
4. If $rand < \exp[-\Delta E/k_B T]$, accept the spin rotation
5. Go to the next site and go to (2)
6. If all sites in the simulation box have been visited, go to (1).

The steps (1)-(6) repeat as many MC steps are considered. Regarding the changes in the moment, here Heisenberg spins are considered, hence any rotations in the unity sphere are allowed.

The Metropolis algorithm can be used to obtain properties of the system related to magnetization $\vec{M} = \sum m_i \hat{e}_i$ averages, such as magnetic susceptibility and heat capacity. Due to finite size effects, the Curie temperature (T_C) of ferromagnet can be obtained by the Binder cumulant, given by

$$U_4 = 1 - \frac{1}{3}\frac{\langle M^4 \rangle}{\langle M^2 \rangle^2} \tag{4.16}$$

where $M = |\vec{M}|$. The intersection of U_4 for different simulation cell sizes can be then used to determine T_C [80], as illustrated in Fig. 4.2.

4.3 Spin waves

For a ferromagnet, the ground state is the state of maximum polarization. Thus, low energy excitations can be created by inverting the atomic spin of a given site i in the spin chain, see Fig. 4.3. The direct consequence is the

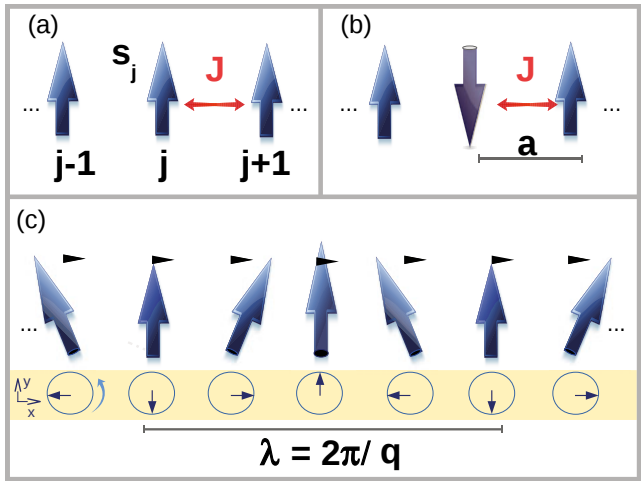

Figure 4.3. Ferromagnetic spin chain: ground state (a), inversion of a spin (b) and ferromagnetic spin wave (c).

decrease in magnetization, in this case 1 μ_B. However, this perturbation propagates in the chain in the form of collective excitations called spin waves (Fig. 4.3).

By analogy with classical mechanics, we can relate the spin moment to the angular momentum $\vec{L}$. The time evolution of $\vec{L}$ is given by

$$\frac{d\vec{L}}{dt} = \mathscr{T}, \tag{4.17}$$

in which $\mathscr{T}$ is the torque. In the classical approximation each spin moment in a chain is under the action of a molecular field (or exchange field) $\vec{H}_j$ due to the coupling J_{ij} of the spin moments $\vec{s}_j$ with the moments $\vec{s}_i$ of the neighborhood. Thus, $\vec{H}_j$ can be considered as a local effective magnetic field that exerts a torque in $\vec{m}_j$, collaborating for the magnetic ordering of the ground state. Therefore, by the Heisenberg Hamiltonian, follows

$$\mathscr{H} = -\frac{1}{2}\left[\sum_{i\neq j} J_{ij}\vec{m}_i\right]\cdot\vec{m}_j = -\frac{1}{2}\gamma\vec{H}_j, \tag{4.18}$$

with γ the gyromagnetic ratio. In a chain of spins, Fig. 4.3, each j site has 2 first neighbors $j-1$ and $j+1$. The time evolution of $\vec{m}_j$ will be

$$\begin{aligned}\frac{d\vec{m}_j}{dt} &= \vec{m}_j \times \vec{H}_j \\ &= -\gamma J\left[\vec{m}_j \times \vec{m}_{j-1} + \vec{m}_j \times \vec{m}_{j+1}\right].\end{aligned} \tag{4.19}$$

It follows that for each component,

$$\frac{dm_j^x}{dt} = J[(m_{j-1}^z + m_{j+1}^z)m_j^y - (m_{j-1}^y + m_{j+1}^y)m_j^z], \tag{4.20}$$

$$\frac{dm_j^y}{dt} = J[-(m_{j-1}^z + m_{j+1}^z)m_j^x + (m_{j-1}^x + m_{j+1}^x)m_j^z], \tag{4.21}$$

$$\frac{dm_j^z}{dt} = J[(m_{j-1}^y + m_{j+1}^y)m_j^x - (m_{j-1}^x + m_{j+1}^x)m_j^y]. \tag{4.22}$$

For small perturbations transverse to spin we can approximate $m_j^z \approx m_j$ and $m_j^x, m_j^y << m_j$. Thus, Eq. 4.20-4.22 turn into

$$\frac{dm_j^x}{dt} = Jm_j[2m_j^y - m_{j-1}^y - m_{j+1}^y)], \tag{4.23}$$

$$\frac{dm_j^y}{dt} = -Jm_j[2m_j^x - m_{j-1}^x - m_{j+1}^x)], \tag{4.24}$$

and

$$\begin{aligned}\frac{dm_j^z}{dt} &= J[(m_{j-1}^y + m_{j+1}^y)\underbrace{m_j^x}_{\approx m_j^y} - (\underbrace{m_{j-1}^x}_{\approx m_{j-1}^y} + \underbrace{m_{j+1}^x}_{\approx m_{j+1}^y})m_j^y] \\ &= 0. \end{aligned} \tag{4.25}$$

To solve Eq.4.23 and Eq.4.24 we use the following plane wave *ansatz*:

$$m_j^x = Am_j e^{i(jqa-\omega t)} \tag{4.26}$$

and

$$m_j^y = Bm_j e^{i(jqa-\omega t)}, \tag{4.27}$$

where a is the inter-atomic distance and q is the modulus of the wave vector. By replacing Eq. 4.26 and Eq.4.27 in Eq. 4.23 and Eq. 4.24, respectively, results

$$-iA\omega = 2BJm_j[1-\cos(qa)]. \tag{4.28}$$

and

$$-iB\omega = -2AJm_j[1-\cos(qa)]. \tag{4.29}$$

Therefore,

$$\begin{pmatrix} i\omega & 2Jm_j[1-\cos(qa)] \\ 2Jm_j[1-\cos(qa)] & -i\omega \end{pmatrix} \begin{pmatrix} A \\ B \end{pmatrix} = \begin{pmatrix} 0 \\ 0 \end{pmatrix}. \tag{4.30}$$

For a solution other than trivial, it follows that

$$\begin{vmatrix} i\omega & 2Jm_j[1-\cos(qa)] \\ 2Jm_j[1-\cos(qa)] & -i\omega \end{vmatrix} = 0 \tag{4.31}$$

$$\begin{aligned} \omega &= 2Jm_j[1-\cos(qa)] \\ &= 4Jm_j \sin^2(qa/2). \end{aligned} \tag{4.32}$$

For $q << 1$, in regions near the center of the first Brillouin zone $\sin(qa) \approx qa$,

$$\omega \approx Dq^2 \tag{4.33}$$

The Eq.4.33 is the spin waves dispersion for a ferromagnetic material, in which $D = Jm_j a^2$ is the stiffness constant. Note that D is specific to each material since it depends on J. Equation 4.33 can be generalized for cubic lattices, however its characteristic q^2 behaviour remains.

The approximation of $q << 1$ can also be understood as low energy. Therefore, Eq. 4.33 shows that a small amount of energy is associated with high wavelength excitations ($\lambda = 2\pi/q$). Thus the lower energy excited states can be understood as the spin reversal ($\uparrow\uparrow\uparrow\downarrow\uparrow\uparrow\uparrow$) smeared in the form of wave in the spin chain.

4.3.1 Adiabatic magnon spectra

Other method to compute the spin wave dispersion is to Fourier transform the calculated exchange parameters J_{ij}. That results in the so-called adiabatic magnon spectrum. In the case of one atom per cell, the energy of a spin wave with respect to a ferromagnetic ground state is given by

$$E(\vec{q}) = \sum_{j\neq 0} J_{0,j} \left[\exp\left(i\vec{q} \cdot \vec{R}_{0,j} \right) - 1 \right] \tag{4.34}$$

where $\vec{R}_{0,j}$ is the relative position vector connecting sites i and j. From this it is straightforward to calculate the spin wave dispersion $\omega(q)$ [39]. For systems with more than one atom per cell, as is the case for elements with hcp crystal structure, alloys or thin films consisting of more than one monolayer, the spin wave energies are given by the eigenvalues of the general N×N matrix, here expressed in block form

$$\begin{pmatrix} \sum_n^N J_0^{ln} - J^{ll}(\vec{q}) & -J^{ln}(\vec{q}) \\ -J^{ln}(\vec{q})^* & \sum_n^N J_0^{nl} - J^{nn}(\vec{q}) \end{pmatrix}, \tag{4.35}$$

where N is the number of atoms per cell and l, n are indices for different atoms in the cell. The adiabatic magnon spectra (AMS) relies in the adiabatic approximation in which the slow motion of the spins is decoupled from the fast

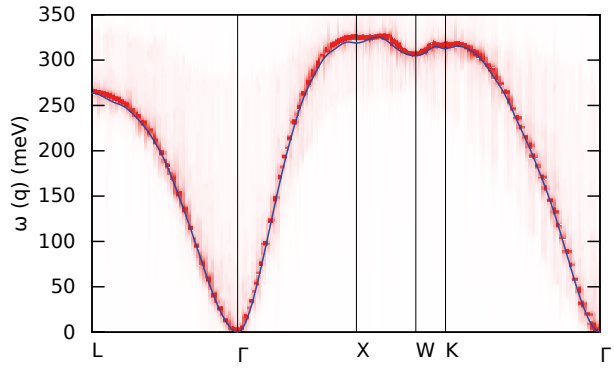

Figure 4.4. Adiabatic magnon spectra (blue line) and the S(q,ω) for a ferromagnetic material, here fcc Ni.

motion of the itinerant electrons. Therefore, it is suitable to represent low energy excitations and for systems with reasonably large exchange splitting [81]. As illustration, in Fig. 4.4 is plotted the AMS for a ferromagnetic material, showing the characteristic quadratic dispersion around Γ point.

Noncollinear spin wave theory

Recently, the adiabatic magnon spectra were derived within the linear spin wave theory (LSWT) frame for a noncollinear ground-state magnetic structure, following a strategy similar to that described elsewhere [82]. For the case of non-collinear spin order, in which the crystallographic unit cell is commensurate with the magnetic cell, we can defined a local coordinate system that transforms the non-collinear configuration into FM order, by applying a rotation $\mathscr{R}$ on every moment within the crystallographic unit cell. This rotation is applied to the spin Hamiltonian described by Eq. 4.8, considering that the $\hat{m}_i, \hat{m}_j$ are pseudospin-1/2 operators, and provides :

$$\begin{aligned}\mathscr{H} = \quad & \sum_{ij}\left(\sqrt{\tfrac{m_i}{2}}(\bar{\mathbf{u}}_i^{\mathrm{T}} a_i + \mathbf{u}_i^{\mathrm{T}} a_i^{\dagger} + \mathbf{v}_i^{\mathrm{T}}(m_i - a_i^{\dagger} a_i))\right) \mathscr{J}_{ij} \\ & \left(\sqrt{\tfrac{m_j}{2}}(\bar{\mathbf{u}}_j^{\mathrm{T}} a_j + \mathbf{u}_j^{\mathrm{T}} a_j^{\dagger} + \mathbf{v}_j^{\mathrm{T}}(m_j - a_j^{\dagger} a_j))\right), \end{aligned} \tag{4.36}$$

where $a_i^{\dagger}/a_i$ are bosonic operators that decrease/increase the spin quantum number and s_i is the modulus of the classical spin vector at atomic position i. The vectors $\mathbf{u}_i$ and $\mathbf{v}_i$ are defined in terms of the rotation matrix $\mathscr{R}$ by using the Rodriguest' formula

$$\begin{aligned} u_i^{\beta} &= \mathscr{R}_i^{\beta 1} + i\mathscr{R}_i^{\beta 2}, \\ v_i^{\beta} &= \mathscr{R}_i^{\beta 3}, \end{aligned} \tag{4.37}$$

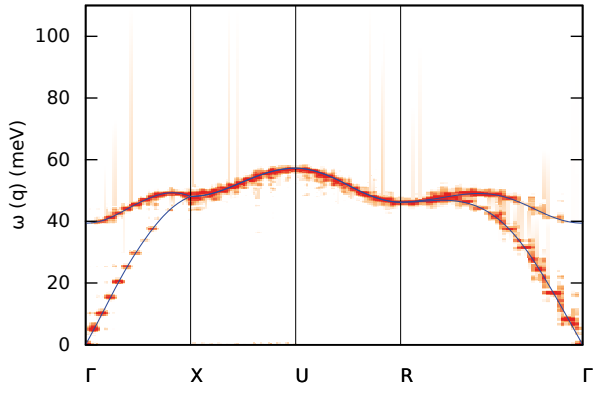

Figure 4.5. Adiabatic magnon spectra (blue line) computed by non-linear spin wave theory and the S(q,ω) for a G-type antiferromagnetic material, here $CaMnO_3$ bulk. Due to small distortions of the lattice, the two magnon branches are not degenerated around the Γ point.

where β runs over $\{x,y,z\}$. The exchange tensor $\mathscr{J}_{ij}$ reads

$$\begin{aligned}\mathscr{J}_{ij} &= J_{ij}\mathscr{I} + \mathscr{J}^S_{ij} + \mathscr{J}^A_{ij} \\ &= \begin{pmatrix} J_{ij}+\Gamma^{xx}_{ij} & D^z_{ij} & -D^y_{ij} \\ -D^z_{ij} & J_{ij}+\Gamma^{yy}_{ij} & D^x_{ij} \\ D^y_{ij} & -D^x_{ij} & J_{ij}-\Gamma^{xx}_{ij}-\Gamma^{yy}_{ij} \end{pmatrix}. \end{aligned} \tag{4.38}$$

After Fourier transform, the Hamiltonian in Eq. 4.36 can be recast in the following form :

$$\mathscr{H} = \sum_{k\in \mathrm{BZ}} \begin{pmatrix} a^\dagger_i(\mathbf{k}) a_i(-\mathbf{k}) \end{pmatrix} \begin{pmatrix} A(\mathbf{k})-C & B(\mathbf{k}) \\ B^\dagger(\mathbf{k}) & \bar{A}(-\mathbf{k})-C \end{pmatrix} \begin{pmatrix} a_i(\mathbf{k}) \\ a^\dagger_i(-\mathbf{k}) \end{pmatrix},$$

where A, B, and C are defined as :

$$A(\mathbf{k})_{ij} = \frac{\sqrt{m_i m_j}}{2} \mathbf{u}_i^{\mathrm{T}} \mathscr{J}_{ij}(-\mathbf{k}) \bar{\mathbf{u}}_j, \tag{4.39}$$

$$B(\mathbf{k})_{ij} = \frac{\sqrt{m_i m_j}}{2} \mathbf{u}_i^{\mathrm{T}} \mathscr{J}_{ij}(-\mathbf{k}) \mathbf{u}_j, \tag{4.40}$$

$$C(\mathbf{k})_{ij} = \delta_{ij} \sum_l m_l \mathbf{v}_i^{\mathrm{T}} \mathscr{J}_{il}(0) \mathbf{v}_l. \tag{4.41}$$

This is diagonalized by using a Bogoliubov transformation [83]. The calculated eigenvalues are the eigenfrequencies of the spin waves and are plotted in Fig. 4.5 for an antiferromagnetic material, showing the characteristic linear dispersion around Γ point.

4.3.2 Dynamical structure factor S(q,ω)

For dynamical properties, a reformulation of the LLG equation in the spirit of Langevin dynamics must be performed as in Eq. 4.12. In this way, it is possible to obtain the dynamic properties of the system, such as time evolution of the magnetization and the spatial and time correlation function of the magnetic moments,

$$C^k(\vec{r}-\vec{r'},t,t') = \langle m_r^k(t)\, m_{r'}^k(t')\rangle - \langle m_r^k(t)\rangle\, \langle m_{r'}^k(t')\rangle \;, \tag{4.42}$$

where $\langle\ \rangle$ stands for the ensemble mean average and k the Cartesian components. The time and space Fourier transform of Eq. 4.42 is the dynamical structure factor S($\vec{q}$,ω), given by

$$S^k(\vec{q},\omega) = \frac{1}{N}\sum_{\mathbf{r},\mathbf{r'}} e^{-i\vec{q}\cdot(\vec{r}-\vec{r}')}\int_{-\infty}^{\infty} e^{i\omega t} C^k(\vec{r}-\vec{r}',t)\, dt \;, \tag{4.43}$$

where N is the number of terms in the sum, $\vec{q}$ and ω are the moments and energy transfer. In this way, the magnon spectra is obtained by gathering the positions of the peaks of the dynamical structure factor along a particular direction in the reciprocal space [26, 27] which is in accordance with the adiabatic approximation since they are neglected longitudinal fluctuations of the atomic spins in the simulations.

5. Introduction to the papers

This chapter is dedicated to summarize the main results of the papers contained in this thesis. The magnetism of bulk, thin films and nanostructures adsorbed on surfaces system were studied with main focus on the ground state properties and magnetization dynamics.

My contributions in each work is described below.

Bulk Systems

In Paper **I** I performed all calculation of critical temperatures and magnons for the heavy rare-earths using atomistic spin dynamics and Monte Carlo method.

In Paper **II** I performed electronic structure calculations using the RS-LMTO-ASA for the Permalloy VCA and local clusters of Fe-Ni. I also was responsible by the post processing, that was dedicated to compute the local anisotropies by Bruno's formula.

Thin films

In Paper **III** I performed all electronic structure calculations using the RS-LMTO-ASA, including the calculations of the exchange parameters. I also performed the atomistic spin dynamics for the $Fe_6/Ir(001)$ surface magnons.

In Paper **IV** I performed the atomistic spin dynamics in order to obtain the magnon spectra, as well as the MC simulations for the critical temperatures of fcc Ni and Ni surfaces on Cu(001) and Cu(111).

Nanostructures adsorbed on surface

In Paper **V**, I performed electronic structure calculations using the RS-LMTO-ASA for the Pd(111) surfaces and Cr nanostructures on Pd(111). I was engaged in this project since the very initial stage and I also contributed to conceive the idea.

Additionally, for all papers listed above, I participated of the discussion of the results and also contributed to the manuscripts preparation.

5.1 Rare earth's magnons

In paper **I**, the applicability of the Hubbard I approximation is examined (in connection with a full-potential electronic structure method) and how this method reproduces cohesive, structural, and magnetic properties, as well as spectroscopic data, of the rare-earth series. In general a good agreement between theory and observations is found, where a comparison can be made. In

particular, it is rewarding that equilibrium volumes, bulk moduli, and magnetic properties are in good agreement with measured data. Similarly, calculated magnetic excitations as well as photoelectron spectra (direct and inverse) are in good agreement with measured data. As to the 4f magnetic moment we obtain similar values as would be obtained from a Russel-Saunders ground state. It is rewarding that this follows as a natural result from a quantum mechanical treatment that makes no assumption of the mechanism of coupling angular momentum states. This paper also points out shortcomings of other methodologies, like local density approximation (LDA) and LDA + U, in establishing results that consistently agree with measurements. In particular, the electronic structure from these theories is found to not reproduce the measured x-ray photoemission spectroscopy and Bremsstrahlung isochromat spectroscopy spectra, while the Hubbard I approximation gives a very satisfactory account of the measured spectra. Among the different methods considered here, the treatment of the 4f shell as part of a non-hybridizing core comes closest to the Hubbard I approximation, since the LDA + U approximation is found to overestimate the hybridization and results in formation of dispersive energy states. The 4f states were treated in the core with a Russel-Saunders ground state. The resulting exchange parameters give ordering temperatures and magnon dispersion that are in acceptable agreement with measurements. The 4f-induced polarization of the [spd]-valence band states is also captured with this 4f in the core treatment, a poor-man's version of the Hubbard I approximation. The Hubbard I approximation is hence demonstrated to be consistent with the standard model of the lanthanides, which identifies the 4f shell as atomiclike, and provides practical and reliable theoretical framework of the rare-earth elements and rare-earth-containing materials in general. This opens for accurate theoretical analysis of rare-earth-containing multiferroics, rare-earth-based permanent magnets, rare-earth-based topological insulators, and rare-earth-based photovoltaics. Although it seems that the HIA is, among the available state-of-the-art methods, the most promising for the REs, a correct assessment of the magnetic anisotropy and related quantities remains a challenge. These quantities strongly depend on the subtle balance between the crystal field and the spin-orbit coupling.

The ordering temperature TN/C for the heavy RE metals was estimated by means of Monte Carlo simulations and using the cumulant crossing method. To do these calculations, we used the values of the exchange parameters and magnetic moments from DFT. The Hamiltonian used to estimate the ordering temperature is described by Eq. (6) in Paper I but neglecting the anisotropy term. The results were compared with the simple estimates, based on mean-field approximation (MFA). We underline the fact that due to the long-range nature of the magnetic couplings, a relatively large number of exchange interactions was required in order to sufficiently converge the TN/C value. For most of the simulations we had to include the Jijt's with all nearest neighbours (NN) within the distance of 5.57 lattice parameters, which corresponds to taking into

account the nearest 1098 neighbours of each atom. The magnon spectrum of Gd was simulated with ASD, using a low-temperature experimental value of the uniaxial anisotropy constant $K_1 = 2.5$ μRy. A simulation box containing 50x50x50 sites with periodic boundary conditions was adopted. The temperature was set to T = 78, the damping parameter to $\alpha = 0.001$. Moreover, the exchange interaction were taken with all neighbours within a maximum distance of $5.57a$, where a is the lattice parameter.

5.2 Anisotropy in Permalloy

In paper **II**, the microscopic origin of the vanishingly low magnetic anisotropy of Permalloy (Py) was investigated by using relativistic first-principles calculations. The magnetic anisotropy of a macroscopic sample was considered here as a configurational average of local anisotropies, for a diverse distribution of clusters containing 19 atomic sites of the fcc lattce. Each cluster may have several atoms with large local anisotropies directed in any of the common crystallographic axes ($\langle 001 \rangle$, $\langle 110 \rangle$ and $\langle 111 \rangle$), but since the inter-atomic exchange interaction of Py is much stronger and ferromagnetic, the resulting magnetic configuration is a collinear ferromagnet, where, after a proper configurational average is made, the resulting MAE is expected to be vanishingly small. In the presented study, only clusters with approximately the same concentration of Py ($Fe_{0.2}Ni_{0.8}$) were investigated. In a real sample such constrain does not exist, and configurations involving, e.g., 1 Ni and 18 Fe atoms and vice-verse must also be considered. Once a proper configurational average of a huge set of clusters is considered, the proper macroscopic MAE can be obtained, and it is suggested this leads to a vanishingly small MAE for Py. The scenario proposed here is principally different than simply making a linear interpolation of anisotropy constants of bcc Fe and fcc Ni and adopting an interpolated value for all atoms of the alloy. In the current paper, It was proposed that the low magnetic anisotropy of Py is intrinsically related to the local symmetries of the alloy. It was shown that the local magnetic anisotropy of individual atoms in Permalloy can be several orders of magnitude larger than that of the bulk sample, and 5-10 times larger than that of elemental Fe or Ni. It is, furthermore, show that locally there are several easy axis directions that are favoured, depending on local composition. The results are discussed in the context of perturbation theory, applying the relation between magnetic anisotropy and orbital moment. Permalloy keeps its strong ferromagnetic nature due to the exchange energy to be larger than the magnetocrystalline anisotropy. As a final comment, note that the local anisotropy effects discussed here might affect the magnetization dynamics in thin films of Py. For that, adopting a scenario of locally unique information, as proposed in Paper **II**, would be relevant for the interpretation of pump-probe measurements and crucial to simulations involving an effective spin-Hamiltonian.

5.3 Magnon softening on Fe_6/Ir(001) surface

In Paper **III**, it is evaluated how thermal effects soften the magnon dispersion in 6 layers of Fe(001) on top of Ir(001). In order to do that, a systematic study was performed considering a noncollinear spin arrangement to calculate configuration-dependent exchange parameters. In addition, Monte Carlo simulations were performed in order to estimate the noncollinear spin arrangement as a function of temperature. Hence, the noncollinear exchange couplings related to these configurations were calculated and used in an atomistic spin dynamics approach to evaluate the magnon spectra. Good agreement was obtained with experimental measurements of the acoustic magnon dispersion, even though only a one-shot approach was employed where mean angles that indicates the deviation from ferromagnetic order is obtained from atomistic spin dynamics simulations using exchange parameters from a ferromagnetic solution, and new exchange integrals were evaluated from ab initio theory with these angles. The finite-temperature variations in the exchange coupling are found to be significant, and it is proposed in Paper III that this is a important contribution to the magnon softening observed in the Fe/Ir(001) system.

5.4 Surface magnons and critical temperatures at Ni surfaces

In Paper **IV**, the magnetic moments and exchange interactions for Ni surfaces on Cu substrate in the cleavage directions $\langle 001 \rangle$ and $\langle 111 \rangle$ are computed. It is shown that the Ni ions at the interface experience a reduction of their magnetic moments and exchange interactions. These two trends tend to compensate each other because of the form of the Heisenberg Hamiltonian, where the magnitude of the moment is contained within the exchange couplings. The middle layers of Ni in the case of 9ML have characteristics similar to Ni-bulk. Regarding the spin dynamics simulations, an excellent agreement of the magnon dispersion is found for Ni bulk compared with experiments. The acoustic branch of the adiabatic magnon spectra is affected by the differences in coordination number of different surface directions. This feature can be noticed in the exchange stiffness. Further studies are necessary in order to track the film thickness necessary to recover bulk magnons.

The ordering temperature T_C was estimated for Ni bulk and surfaces by means of Monte Carlo simulations using the peak of susceptibilities. The Hamiltonian used in the simulations is the one described by Eq. (1) in Paper **IV**. The results were compared with mean-field approximation estimations. The results indicate that mean-field approximation-based estimations fail compared with the ones obtained with Monte Carlo methods. One can also see that the calculated ordering temperatures for Ni layers obtained with Monte Carlo simulations, in general, agree with a 1/n trend, however the values are underes-

timated with respect to the experimental data. The largest errors in the Monte Carlo calculation are found for Ni bulk which is about half of the experimental values. This is related to the fact that we neglect longitudinal fluctuations.

5.5 Magnetism of Cr nanostructures on Pd(111)

In paper **V**, the electronic structure, magnetic moments (spin and orbital) and exchange interactions (both Heisenberg and Dzyaloshinskii-Moriya type) of various sizes and shapes of Cr clusters on a Pd(1 1 1) substrate were reported. We find in general that the magnetic moments are sizeable, almost entirely of spin-character and strongly affected by the hybridization with other surrounding Cr atoms. In general, we find that the Cr atoms induce spin polarization on Pd sites localized nearby the nanostructure but with an small magnetization. The local density of states (LDOS) figures also show that for one dimensional clusters, the peaks are very narrow. This is a characteristic of systems with reduced symmetry and low dimensionality as in the case of isolated atoms while for 2D systems, the LDOS become broader and span over a wider energy range.

It is also found that the interactions in all clusters is dominated by nearest-neighbor antiferromagnetic Heisenberg form, with a strength of -6.0$\pm$0.5 mRy. This conclusion holds for both one- and two-dimensional clusters, with the only exception being the dimer, where the interaction is somewhat stronger. This implies that Cr on Pd(1 1 1) forms an ideal model system, in which clusters of almost any shape and size can be investigated from a Heisenberg Hamiltonian, using a nearest-neighbor exchange model with a strength of the interaction equal to -6.0 mRy. Both static and dynamic effects of Cr clusters on Pd(1 1 1) should hence be possible to investigate with a rather accessible model. Finally, we have found that complex magnetic structures can be realized for linear chains of Cr, something which is due to a competition between exchange interaction and the much weaker Dzyaloshinskii-Moriya term. In particular, two different magnetic states with very similar energy can be stabilized; one collinear antiferromagnetic structure and one with an antiferromagnetic spin-density wave. This result can have very interesting technological applications for magnetic switching. Since both states are similar in energy, the switching between both magnetic configurations is low-energy cost.

6. Summary and outlook

In this thesis, I discussed the magnetism of diverse magnetic materials in solid state. As examples were shown the bulk properties from elemental rare-earths and Fe-Ni random alloy, the thin films of Fe and Ni supported in a non-magnetic substrate and Cr nanostructures adsorbed on a substrate with considerable spin-orbit interaction. The studies were conducted by using the density functional theory, specially the Real Space Linear Muffin-tin Orbitals in Atomic Sphere Approximation method, and Atomistic Spin Dynamics simulations.

In the first study, I verified that the electronic structure of Gd is well represented even if considering the $4f$ electrons not hybridizing with the conduction electrons. For this reason, the computed magnon dispersion, considering exchange interaction up to 23rd next neighbors, it is in agreement with the neutron scattering experiments [84]. The long ranged J_{ij}'s are also important to capture the pitch vector for Er and Tm, obtained by non-linear spin wave theory. The critical temperatures, computed by Monte Carlo simulations, nicely reproduced the qualitative trend of lowering of the critical temperatures across the series, in spite of quantitative underestimations for some rare earths.

Still on bulk systems, in the second study presented, I showed a discussion about the microscopic mechanism of the vanishingle low magnetic anisotropy of Permalloy using the concept of the orbital moment anisotropy for Fe and Ni atoms in the alloy. I studied clusters with 19 atoms, chosen according to the most probable ones given by the binomial distribution, while keeping the constrain of Permalloy composition. I showed that the anisotropy energy of each atom could be larger (1-3 μRy in average) even though no clear trend regarding configurations *versus* anisotropy was found. I expect that such highly anisotropic landscape could affect dynamical properties of very thin Permalloy films, which requires further investigations.

The third study discussed the magnetism of Fe_6/Ir(001) surface. I performed electronic structure calculations for such system and obtained the J_{ij} considering the FM state, verifying that their values were consistent with those of experimental measurements [18]. By means of the mapping of angular deviations of the spin moments with respect to z-direction into temperature, I noticed a decrease of the first neighbors J_{ij} with temperature for this system. Thus, this gives a more accurate description of magnons at finite temperature in comparison with the experimental data. I propose that this approach could be applied for other $3d$ transition metals magnetic layers, giving room for additional studies.

In the fourth study, I also studied surface magnons for 3 and 9 Ni monolayers on Cu(001) and Cu(111) in order to track the significant surface and/or interface effects and contrast to fcc Ni bulk-like properties. Complementary, I used the Monte Carlo method to estimate the critical temperatures of Ni overlayers in Cu, and recovered the inverse of film thickness dependence seen experimentally, but with underestimated T_C values, specially for fcc Ni. In a future work the longitudinal fluctuation must be considered.

Finally, in the fifth study I investigated the Cr structures on the Pd (111) surface and found that the J_{ij}'s for Cr nearest-neighbors are always antiferromagnetic, with a strength of 6.0 ± 0.5 mRy. This conclusion holds for both one- and two-dimensional clusters. Due to this, for linear structures with few atoms a collinear magnetic configuration is more stable while, for the nanoislands, the magnetization is noncollinear as a result of geometric frustration. For 10 and 24-atom linear nanowires a canted antiferromagnetic configuration has been found. This is occasioned by the interaction with the Pd substrate and possibly the interaction of Dzyaloshinsky-Moriya. For future studies I have special interest in antiferromagnetic dynamics and Cr on Pd(111) is an ideal model system, in which clusters of almost any shape and size can be investigated from a Heisenberg Hamiltonian, using a nearest-neighbor exchange model with a strength of the interaction equal to 6.0 mRy, while some relativistic effects would also be addressed by Dzyaloshinsky-Moriya interaction.

It must be emphasized that the materials investigated in this thesis are directly related to experimental research carried out in the last years and, therefore, I hope that our results contribute to increase the theoretical understanding of magnetism at the nanoscale.

7. Sammanfattning på svenska

I det tjugonde århundradet avslöjade kvantmekaniken den djupaste hemligheten om magneter: spinnet hos elektronen. Många namn kan nämnas, men Pauli, Dirac, Fermi, Heisenberg, Bloch och Néel har definitivt givit de mest inflytelserika bidragen till teorin om metaller och magnetism. Även utvecklingen av täthetsfunktionalteori av Hohenberg och Kohn var en vändpunkt i teoretiska förutsägelser om materialvetenskap. De första tillämpningarna av magnetiska media (magnetband och lagrings diskar) dök upp på 1930-talet. Men det stora genombrottet när det gäller informations teknik kom 1988 med upptäckten av jättemagnetoresistans (GMR) [3, 4] och födelsen av spinntronik vid slutet av nittonhundratalet. Detta har möjliggjort utvecklingen av snabbare teknologi för datalagring och bearbetning.

Nuförtiden går området för magnetisk lagring i en riktning där man vill stabilisera bitarna med minsta antal atomer och med en optimering och bearbetning av dessa, med minsta möjliga energiförbrukning. Man bör komma ihåg att i början av 1990-talet hade hårddiskar en lagringskapacitet på c:a 2 gigabyte, och utvecklingen till nuvarande lagringskapacitet med en terabyte på en hårddisk med vikten 200 gram, har varit enorm.

Utvecklingen inom experimentella tekniker har en betydande roll för forskning om magnetiska material. Till exempel, sveptunnelmikroskop (STM) [6, 7] möjliggör en topologisk kartläggning av ytan på atomär skala, till och med möjligheten med manipulering av atomer. Den har också vissa förfinade tillämpningar, så som spinn-polariserad STM (SP-STM) [8], som ger information om icke-kolinjära magnetiska texturer [9, 10, 11]. Dessutom, sveptunnelspektroskopi (STS) teknik, är i stånd till att kvantifiera den magnetiska kopplingen mellan atomer [14]. Det är också möjligt att undersöka kollektiva magnetiska excitationer i ett magnetiskt material (magnoner) medelst inelastisk neutronspridning (INS) [15, 16, 17] och s.k. Spin Polarized Electron Energy Loss Spectroscopy (SPEELS) [18]. Med användningen av dessa experimentella metoder har man nyligen visat på möjligheten att stabilisera bitar sammansatta av så lite som endast 12 atomer [20] och nanokomponenter som utför logiska operationer har demonstrerats endast med atomära spinn [21]. Användningen av neutron- och elektronspridningstekniker möjliggör att man kan mäta magnon dispersionen vilket ger tillgång till värdefull information om det studerade materialet såsom utbyteskoppling, magnetisk anisotropi och eventuellt Dzyaloshinsky-Moriya interaktion. Det betyder, att man bättre kan förstå magnetism vilket möjliggör teknologier att skapa nya logiska enheter, till exempel magnon transistorer [19].

Därför, med hänsyn till dessa perspektiv och högt vetenskapligt intresse på området för nanomagnetism, presenteras i denna avhandling teoretiska studier av elektronstruktur och atomär spin-dynamik av magnetiska material. Arbetet har utförts med hjälp av första princip beräkningar och den s.k. *Real-Space Linear Muffin-Tin Orbitals within Atomic Sphere Approximation* metoden (RS-LMTO-ASA) [22, 23, 24] och *Uppsala Atomistic Spin Dynamics* kod (UppASD) [26, 27].

För material med bulkegenskaper, utvärderade vi den kritiska temperaturen och magnon spektra av de tunga sällsynta jordartsmetallerna: Gd, Tb, Dy, Ho, Er och Tm. Med hjälp av utbytesväxelverkansparametrar och magnetiska moment, erhållna från första-princip beräkningar utförde vi Monte Carlo-simuleringar och kunde på så sätt återge kvalitativa värden av trenden hos den kritiska temperaturerna, över serien. Förutom bulksystem, innehåller denna avhandling an analys av den mikroskopiska mekanismen hos det försvinnande låga magnetiska anisotropin av Permalloy. Detta gjordes med hjälp av en atomär uppdelning av anisotropin för Fe och Ni-atomer i legeringen. Relaterade till ytans magnetism, har vi diskuterat användningen av utbytesväxelverkansparametrar som, beräknats i en icke-kolinjär formalism för 6 monolager av Fe på ett Ir (001) substrat. Denna ytstudie motiverades med för att få en mer exakt beskrivning av magnoner vid ändlig temperatur, och möjliggjorde en direkt jämförelse med experimentella data. Vi har i denna avhandling dessutom studerat magnoner på 3 och 9 Ni-monolager på Cu (001) och Cu (111), för att spåra signifikanta yt- och/eller gränssnitts effekter hos dessa kollektiva excitationer, och att kontrastera detta till egenskaper som är fcc Ni bulk-liknande. Dessutom använde vi Monte Carlo simuleringar för att uppskatta de kritiska temperaturerna av Ni-ytor och jämför dessa med experimentella data. Slutligen, låg dimensionell magnetism, presenterar vi ab-initio beräkningar för elektroniska strukturen av Cr-nanostrukturer med olika geometrier, som adsorberas på en Pd (111) yta (se figur 7.1). I denna studie var fokus op formeringen av icke-kolinjära spin konfigurationer, antingen på grund av geometrisk frustration eller som tillhandahålls av växelverkan via substratet.

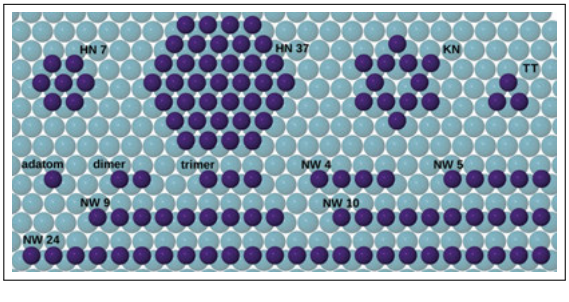

Figure 7.1. Cr-nanostrukturer med olika geometrier, som adsorberas på en Pd (111) yta.

8. Resumo em português

No século XX, a mecânica quântica revelou o segredo mais profundo sobre os ímãs: o *spin* do elétron. Muitos cientistas devem ter seus nomes citados, porém Pauli, Dirac, Fermi, Heisenberg, Bloch e Néel têm definitivamente as contribuições mais influentes para a teoria dos metais e magnetismo. Outro desenvolvimento importante foi a teoria da densidade funcional (DFT acrônimo de *density functional theory*) por Hohenberg e Kohn, que representou um momento decisivo para a investigação teórica na ciência de materiais. Além disso, as primeiras gravações em mídia magnética apareceram na década de 1930, com fitas magnéticas e disquetes. No entanto, com a descoberta da magnetorresistência gigante (GMR)[3, 4], em 1988, culminou no nascimento da spintrônica no final do século passado. Isso permitiu o desenvolvimento de dispositivos mais eficazes para o armazenamento e processamento de dados.

Atualmente, a área de pesquisa em armazenamento magnético tem como horizonte estabilizar bits com o menor número possível de átomos e otimização do processamento, associado a um menor gasto energético. Ao relembrar que no início dos anos 90 os discos rígidos tinham uma capacidade de armazenamento de 2 Gigabytes, pode-se ter a dimensão do comedimento da comunidade científica para atingir os atuais Terabytes em discos rígidos de 200 gramas.

Os recentes desenvolvimentos em técnicas experimentais têm um papel significativo para a pesquisa em materiais magnéticos. Por exemplo, o microscópio de tunelamento quântico (*scanning tunneling microscope* – STM) [6, 7] permite o mapeamento topológico de um superfície com resolução atômica além da manipulação de átomos. Este também conta com algumas aplicações específicas, tais como sua versão spin-polarizada (SP-STM) [8], que permite imageamento do magnetismo não-colinear [9, 10, 11] além da espectroscopia de tunelamento quântico (*scanning tunelling spectroscopy* – STS), que permite medidas do acoplamento magnético entre átomos [14]. Também é possível investigar as excitações coletivas dos spins em um material magnético (magnons) por meio das técnicas de espalhamento inelástico de neutrons (*inelastic neutron scattering* – INS) [15, 16, 17, 16] e além do recente desenvoltimento de uma nova técnica espectroscópica com resolução para investigar filmes finos chamada *Spin Polarized Electron Energy Loss Spectroscopy* – SPEELS [18].

Utilizando técnicas de STM, recentes pesquisas experimentais mostram a possibilidade de estabilizar bits compostos de 12 átomos a baixa temperatura e a construção de nanodispositivos que executam operações lógicas usando apenas spins. De fato, o uso de técnicas de espalhamento de elétrons e nêutrons

para medir a relação de dispersão de magnons garante o acesso a informações valiosas sobre o sistema estudado, como o acoplamento de troca, anisotropia magnética e possivelmente a interação de Dzyaloshinsky-Moriya. Ou seja, o que é essencial para compreender o magnetismo e, subsequentemente, criar dispositivos, tais como transistores baseados em magnons [19].

Os estudos mostram que, apesar de todos os avanços alcançados, a compreensão do nanomagnetismo na matéria, desde o conhecimento básico até as aplicações de alto desempenho, como discos magnéticos de alta densidade de armazenamento e dispositivos baseados em *spintronics* ou *magnonics* são um desafio diário para os cientistas de materiais.

Assim, devido estas perspectivas e alto interesse científico no campo do nanomagnetismo, nesta tese são apresentados estudos teóricos da estrutura eletrônica e da dinâmica do spin atomísticos de materiais magnéticos, realizados por meio de cálculos de primeiros princípios utilizando o método *Real-Space Linear Muffin-Tin Orbitals within Atomic Sphere Approximation* (RS-LMTO-ASA) [22, 23, 24] e o pacote computacional *Uppsala Atomistic Spin Dynamics* (UppASD) [26, 27].

Com relação às propriedades de sistemas *bulk*, avaliamos as temperaturas críticas e o espectro de magnons das terras raras (Gd, Tb, Dy, Ho, Er e Tm). Utilizando os parâmetros de troca e os momentos magnéticos dos cálculos de primeiros princípios, realizamos simulações usando Monte Carlo e obtivemos um bom acordo com a tendência qualitativa de diminuição das temperaturas críticas ao longo da série. Ainda sobre sistemas *bulk*, discutimos sobre o mecanismo microscópico da baixa anisotropia magnética da liga Permalloy usando o conceito da anisotropia de momento orbital para os átomos de Fe e Ni da liga. Sobre o magnetismo em superfícies, discutimos o uso de parâmetros de troca calculados por um formalismo não colinear para as 6 monocamadas de Fe sobre o substrato Ir(001), de modo a ter uma descrição mais precisa dos magnons a temperatura finita, em comparação com dados experimentais. Além disso, estudamos magnons em 3 e 9 monocamadas de Ni em Cu(001) e Cu(111), a fim de diferenciar os efeitos de superfície e/ou interface em contraste as propriedades que são caracteríticas do Ni *bulk*. Por isso, também utilizamos o método de Monte Carlo para estimar as temperaturas críticas das superfícies de Ni e comparar com dados experimentais. Por fim, sobre o magnetismo em baixa dimensionalidade, apresentamos os cálculos *ab-initio* para a estrutura eletrônica de nanoestruturas de Cr em diversas geometrias adsorvidas na superfície Pd(111), com foco na formação de configurações de spin não-colineares, devido à frustração geométrica ou a efeitos do acoplamento de spin-órbita proporcionados pelo substrato.

Acknowledgments

"I... a universe of atoms, an atom in the universe." – Richard Feynman

I found this one of the most beautiful quotes about the humankind facing its own nature. I can extract two important lessons from that. First, that all achievements one may have in life are insignificant compared to the greatness of the universe, and this make us, physicists, charmed by the beauty of nature. Second, that I'm a vast universe myself, made of uncountable particles but also made of many experiences and memories which many people contributed to them. For that, I would like to thank:

- My family, specially my parents Marlene and Olivaldo, that always supported me since I had my first unpretentious questions about nature during my childhood and, principally, when I decided to take the same questions as serious ones, about 12 years ago, and started the incredible journey of been a physicist. I also thank my brother Bruno, my great-aunt Francisca and my Rodrigo for always take care of me and make life a bit more easy and beautiful.
- To my supervisors Prof. Angela Klautau, Prof. Olle Eriksson, Dr. Anders Bergman and Dr. Manuel Pereiro, that very kindly shared their expertise during uncountable discussions during these PhD years. I will be always grateful for your guidance and to believe in my skills.
- To my work partners Corina Etz, Attila Szilva, Yaroslav Kvashnin, Samara Keshavarz, Inka Locht, Danny Thonig, Jonathan Chico and Konstantinos Koumpouras for the discussions and good times in Uppsala.
- To my colleagues from the Physics Department of Federal University of Pará and friends Manoel Neto, Marcelo Ribeiro, Alessandra Braga, Caio Macedo, Tercio Almeida and Jefferson Danilo for sharing this long journey since the undergrad years, master and PhD.
- To my Uppsala friends Daniele Braga, Mauricio Antunes, Adriana Heredia, Fabio Rabelo, Patricia Cordeiro, Carol Rupp, Jonas Anversa, Moyses Araujo, Emilene Leite, João Batista, Nilva Dorini, Dina Perez, Alexis Perez and the group of Brazilian PhD students in Uppsala Ramon Cardias, Filipe Mussini, Luimar Correa, Mailing Bewanger, Giane Damas and Andre Lobato. Thank you for been the sun during the dark days of swedish winter.

References

[1] A. P. Guimaraes. *Revista mexicana de física E*, 50:51, 2004.
[2] P. Hohenberg and W. Kohn. *Phys. Rev.*, 136:B864, 1964.
[3] M. N. Baibich et al. *Phys. Rev. Lett.*, 61:2472, 1988.
[4] G. Binasch et al. *Phys. Rev. B*, 39:4828, 1988.
[5] S. Miastkowski. “when it comes to hard drives, size is everything". http://edition.cnn.com/TECH/computing/9806/12/harddrive.idg/index.html, 1998. Accessed: 2017-04-17.
[6] G. Binnig et al. *Phys. Rev. Lett.*, 49:57, 1982.
[7] D. M. Eigler and E. K. Schweizer. *Nature*, 344:524, 1990.
[8] R. Wiesendanger et al. *Phys. Rev. Lett.*, 65:247, 1990.
[9] S. Heinze et al. *Appl. Phys. A: Mater. Sci. Process.*, 75:25, 2002.
[10] M. Waśniowska et al. *Phys. Rev. B*, 82:012402, 2010.
[11] C. L. Gao, W. Wulfhekel, and J. Kirschner. *Phys. Rev. Lett.*, 101:267205, 2008.
[12] M. Kleiber et al. *Phys. Rev. Lett.*, 85:4606, 2000.
[13] D. H. Wei et al. *Phys. Rev. Lett.*, 103:225504, 2009.
[14] P. Wahl et al. *Phys. Rev. Lett.*, 98:056601, 2007.
[15] J. W. Lynn. *Phys. Rev. B*, 62:5293, 2000.
[16] H. B. Møller and J. C. G. Houmann. *Phys. Rev. Lett.*, 16:737, 1966.
[17] W. C. Koehler et al. *Phys. Rev. Lett.*, 24:16, 1970.
[18] Kh. Zakeri et al. *Nat. Nanotech.*, 8:853, 2013.
[19] A. V. Chumak. *Nat. Commun.*, 5:4700, 2014.
[20] S. Loth et al. *Science*, 335:196, 2012.
[21] A. A. Khajetoorians et al. *Science*, 332:1062, 2011.
[22] P. R. Peduto, S. Frota-Pessôa, and M. S. Methfessel. *Phys. Rev. B*, 44:13283, 1991.
[23] S. Frota-Pessôa. *Phys. Rev. B*, 46:14570, 1992.
[24] A. Bergman et al. *Phys. Rev. B*, 73:174434, 2006.
[25] W. Kohn and L. Sham. *Phys. Rev.*, 140:A1133, 1965.
[26] B. Skubic et al. *J. Phys.: Condens. Matter*, 20:315203, 2008.
[27] A. Bergman et al. *Phys. Rev. B*, 81, 2010.
[28] A. Szilva et al. *Phys. Rev. Lett.*, 111:127204, 2013.
[29] M. Born and J. R. Oppenheimer. *Ann. der Phys.*, 84:457, 1927.
[30] M. Born and K. Huang. *Dynamical Theory of Crystal Lattices*. Oxford University Press, New York, 1954.
[31] L. H. Thomas. *Proc. Cambridge Phil. Roy. Soc.*, 23:542, 1927.
[32] E. Fermi. *Rend. Accad. Naz. Lincei*, 6:602, 1927.
[33] P. A. M. Dirac. *Proc. Cambridge Phil. Roy. Soc.*, 26:376, 1930.
[34] V. von Barth and L. Hedin. *J. Phys. C: Solid State Phys.*, 5:1629, 1972.
[35] J. P. Perdew et al. *Phys. Rev. B*, 46:6671, 1992.
[36] J. P. Perdew, K. Burke, and M. Ernzerhof. *Phys. Rev. Lett.*, 77:3865, 1996.

[37] P. J. Stephens et al. *J. Phys. Chem.*, 98(45):11623, 1994.
[38] V. I. Anisimov, J. Zaanen, and O. K. Andersen. *Phys. Rev. B*, 44:943, 1991.
[39] J. Kübler. *Theory of Itinerant Electron Magnetism*. Oxford Univesity Press, Nova York, 2000.
[40] H. Eschrig. *Optimized LCAO Methods*. Springer, Berlin, 1987.
[41] V. Heine. The pseudopotential concept. In H. Ehrenreich, F. Seitz, and D. Turnbull, editors, *Solid State Physics: Advances in Research and Applications, Vol. 24*, page 1. Academic Press, New York, 1970.
[42] P. E. Blöchl. *Phys. Rev. B*, 50:17953, 1994.
[43] P. Lloyd and P.V. Smith. *Adv. Phys.*, 91B:317, 1972.
[44] O. K. Andersen. *Phys. Rev. B*, 12:3060, 1975.
[45] H. Skriver. *The LMTO Method*. Springer, New York, 1984.
[46] O. K. Andersen, O. Jepsen, and D. Glötzel. *Highlights condensed matter theory*. North Holland, Amsterdam, 1985.
[47] O. K. Andersen, O. Jepsen, and M. Sob. *Linearized Band Structure Methods*. Springer, Nova York, 1987.
[48] R. Haydock, V. Heine, and M.J. Kelly. *J. Phys. C: Solid State Phys.*, 8:2591, 1975.
[49] R. Haydock. The recursive solution of the schrodinger equation. In H. Ehrenreich, F. Seitz, and D. Turnbull, editors, *Solid State Physics: Advances in Research and Applications, Vol. 35*, page 215. Academic Press, Londres, 1980.
[50] N. Beer and D. G. Pettifor. *The Electronic Structure of Complex Systems*. Plenum Press, Nova York, 1984.
[51] H. L. Skriver and N. M. Rosengaard. *Phys. Rev. B*, 43:9538, 1991.
[52] M. Aldén et al. *Phys. Rev. B*, 46:6303, 1992.
[53] P. Mohn. *Magnetism in the Solid State: An Introduction*. Springer, Berlin, 2005.
[54] J. Stöhr and H. C. Siegmann. *Magnetism: From Fundamentals to Nanoscale Dynamics*. Springer, Nova York, 2006.
[55] E. C. Stoner. *Proc. R. Soc. London A*, 165:372, 1938.
[56] M. Menzel et al. *Phys. Rev. Lett.*, 108:197204, 2012.
[57] S. Heinze et al. *Nat. Phys.*, 7:713, 2011.
[58] N. Nagaosa and Y. Tokura. *Nat. Nanotech.*, 8:899, 2013.
[59] M. Pereiro et al. *Nat. Commun.*, 5:4815, 2014.
[60] A. Bergman et al. *Phys. Rev. B*, 75:224425, 2007.
[61] A. I. Liechtenstein et al. *J. Magn. Magn. Mater.*, 67:65, 1987.
[62] S. Frota-Pessôa, R. B. Muniz, and J. Kudrnovský. *Phys. Rev. B*, 62:5293, 2000.
[63] O. Gunnarsson, O. Jepsen, and O. K. Andersen. *Phys. Rev. B*, 27:7144, 1983.
[64] I. Dzyaloshinsky. *J. Phys. Chem. Solids*, 4:241, 1958.
[65] T. Moriya. *Phys. Rev.*, 120:91, 1960.
[66] M. Heide et al. *Spin-orbit Driven Physics at Surfaces - Ψ_k Scientific Highlight Of The Month*, 78:1, 2006.
[67] V. V. Mazurenko and V. I. Anisimov. *Phys. Rev. B*, 71:184434, 2005.
[68] A. Crépieux and C. Lacroix. *J. Mag. Mag. Mat.*, 182:341, 1998.
[69] R. Skomski, A. Kashyap, and A. Enders. *J. Appl. Phys.*, 109(7):07E143, 2011.
[70] P. Bruno. *Phys. Rev. B*, 39:865, 1989.
[71] P. James et al. *Appl. Phys. Lett.*, 76(7):915, 2000.

[72] S. Abdelouahed and M. Alouani. *Phys. Rev. B*, 79:054406, 2009.
[73] O. Eriksson et al. *Phys. Rev. B*, 42:2707, 1990.
[74] C. Andersson et al. *Phys. Rev. Lett.*, 99:177207, 2007.
[75] H. Nyquist. *Phys. Rev.*, 32:110, 1928.
[76] K. Binder and D. P. Landau. *Introduction to modern statistical mechanics*. Oxford University Press, Oxford, 1987.
[77] V. P. Antropov et al. *Phys. Rev. B*, 54:1019, 1996.
[78] O. Eriksson, A. Bergman, L. Bergqvist, and J. Hellsvik. *Atomistic spin dynamics: Foundations and Applications*. Oxford University Press, Oxford, 2017.
[79] J. H. Mentink et al. *J. Phys.: Condens. Matter*, 22:176001, 2010.
[80] K. Binder and D. P. Landau. *A Guide to Monte Carlo Simulation in Statistical Physics*. Cambridge University Press, Cambridge, 2009.
[81] C. Etz et al. *J. Phys.: Condensed Matter*, 27(24):243202, 2015.
[82] S. Toth and B. Lake. *J. Phys.: Condensed Matter*, 27:166002, 2015.
[83] J. H. P. Colpa. *Physica A*, 93(3):327, 1978.
[84] J. Jensen and A. R. Mackintosh. *Rare Earth Magnetism: Structures and Excitations*. Clarendon Press, Oxford, 1991.

Acta Universitatis Upsaliensis

Digital Comprehensive Summaries of Uppsala Dissertations from the Faculty of Science and Technology 1510

Editor: The Dean of the Faculty of Science and Technology

A doctoral dissertation from the Faculty of Science and Technology, Uppsala University, is usually a summary of a number of papers. A few copies of the complete dissertation are kept at major Swedish research libraries, while the summary alone is distributed internationally through the series Digital Comprehensive Summaries of Uppsala Dissertations from the Faculty of Science and Technology. (Prior to January, 2005, the series was published under the title "Comprehensive Summaries of Uppsala Dissertations from the Faculty of Science and Technology".)

Distribution: publications.uu.se
urn:nbn:se:uu:diva-319994

ACTA
UNIVERSITATIS
UPSALIENSIS
UPPSALA
2017